THE GEOLOGICAL SOCIETY OF AMERICA®

Late Pleistocene slip rate of the central Haiyuan fault constrained from optically stimulated luminescence, ^{14}C, and cosmogenic isotope dating and high-resolution topography

Yanxiu Shao[1,2,3,†], Jing Liu-Zeng[1], Jérôme Van der Woerd[4,†], Yann Klinger[3], Michael E. Oskin[5], Jinyu Zhang[6], Peng Wang[6], Pengtao Wang[2], Wei Wang[6], and Wenqian Yao[6]

[1]*Institute of Surface-Earth System Science, Tianjin University, Tianjin 300072, China*
[2]*Gansu Lanzhou Geophysics National Observation and Research Station, Lanzhou 730000, China*
[3]*Institut de Physique du Globe de Paris, Centre National de la Recherche Scientifique, Université de Paris, F-75005 Paris, France*
[4]*Institut de Physique du Globe de Strasbourg, UMR 7516 CNRS, Université de Strasbourg, 5 rue René Descartes, 67084 Strasbourg Cedex, France*
[5]*Department of Earth and Planetary Sciences, University of California, Davis, California 95616, USA*
[6]*Institute of Geology, China Earthquake Administration, Beijing 100029, China*

ABSTRACT

To better constrain the long-term millennial slip rate of the Haiyuan fault in its central part, we revisited the site of Daqing, where there are multiple paired offset terraces. We used 0.1-m-resolution terrestrial light detection and ranging (LiDAR) and uncrewed aerial vehicle imagery to survey the offset terraces, quantify their geomorphology, and map the fault trace. From these observations, we refined the geomorphological interpretation of the site, measured terrace riser offsets, and determined their relation to terrace formation. The well-constrained age of the highest terrace, T3, at 13.7 ± 1.5 ka, determined from a combination of surface and subsurface optically stimulated luminescence, ^{14}C, and terrestrial in situ ^{10}Be cosmogenic radionuclide dating, associated with an offset of 88 m, yields a late Pleistocene minimum slip rate of 6.4 ± 1.0 mm/yr. The less-well-constrained offset (72 ± 3 m) of the T3/T2 riser base and the age (>9.3 ± 0.6 ka) of terrace T2 yield a maximum slip rate of 7.7 ± 0.6 mm/yr. The smallest offset of a gully incised into T1 of 6.0 ± 0.5 m is potentially associated with the most recent slip event that occurred in the last millennia. Overall, these offsets and ages constrain a geological rate of 5–8 mm/yr (preferred rate >6.4 mm/yr), similar to geodetic estimates. Our collocated high-resolution topography and precise chronology make it possible to reveal the geomorphic complexities of terrace riser offsets and their postformational evolution, and to show how previously determined geological rates along the fault were both under- and overestimated.

Yanxiu Shao http://orcid.org/0000-0002-3281-8179

[†]shaoyx@geoidea.org, jerome.vanderwoerd@unistra.fr.

INTRODUCTION

The way in which strain is distributed in the Tibetan-Himalayan orogen is important to characterize in order to understand how continental orogens deform. While north of the Himalayan range, the high southern Tibetan Plateau experiences east-west extension and right-lateral strike-slip faulting, the northern Tibetan Plateau, at lower elevation, is surrounded by large left-lateral strike-slip faults, such as the Altyn Tagh, Kunlun, and Haiyuan faults, and it is affected by active thrusting in the Qilian Shan (Fig. 1; Tapponnier and Molnar, 1977; England and Molnar, 1997). Southeastward from the Qilian Shan, the Haiyuan left-lateral strike-slip fault, the eastern part of which was the site of the A.D. 1920 magnitude M_W 7.9 Haiyuan earthquake with a rupture length of ~230 km (Deng et al., 1984; Ou et al., 2020), becomes the major fault at the northeastern margin of the Tibetan Plateau (Fig. 1). Even though this fault plays an important role in accommodating eastward motion of the northern Tibetan Plateau relative to the Gobi-Alashan to the north (Tapponnier and Molnar, 1977; Gaudemer et al., 1995; Tapponnier et al., 2001a), its rate of slip remains debated.

Overall, decadal geodetic and millennial geological slip-rate studies mostly agree to a rate of 4–10 mm/yr, implying that the Haiyuan fault is the major active fault at the rim of Tibet at this longitude (Li et al., 2009; Daout et al., 2016; Jiang et al., 2017). However, higher slip rates have been documented (Zhang et al., 1988a; Gaudemer et al., 1995; Lasserre et al., 1999, 2002), as well as lower ones (Yuan et al., 1998; Li et al., 2009; He et al., 2010; Jiang et al., 2017; Matrau et al., 2019). Because it has been suggested that the fault slip rate may have changed over time, it is valuable to find multiple slip-rate constraints at a single site to better constrain possible temporal variation (e.g., Sieh and Jahns, 1984; Van der Woerd et al., 1998, 2002).

Terrace risers have commonly been used as markers of fault displacement to constrain slip rates along strike-slip faults (e.g., Lensen, 1968; Weldon and Sieh, 1985; Berryman, 1990; Knuepfer, 1992; Van der Woerd et al., 1998, 2002; McGill et al., 2013). However, terrace risers can seldom be directly dated. One may infer that displacement began to be recorded since the time of upper terrace abandonment, or upon abandonment of the lower terrace (Van der Woerd et al., 2002; Mériaux et al., 2004, 2005; Cowgill, 2007; Zhang et al., 2007). In general, the upper terrace constraints yield a minimum slip rate, while the lower terrace constraint yields a maximum slip rate. Ideally, when terrace ages are not too different, a combination of upper and

https://doi.org/10.1130/B35571.1; 14 figures; 5 tables.

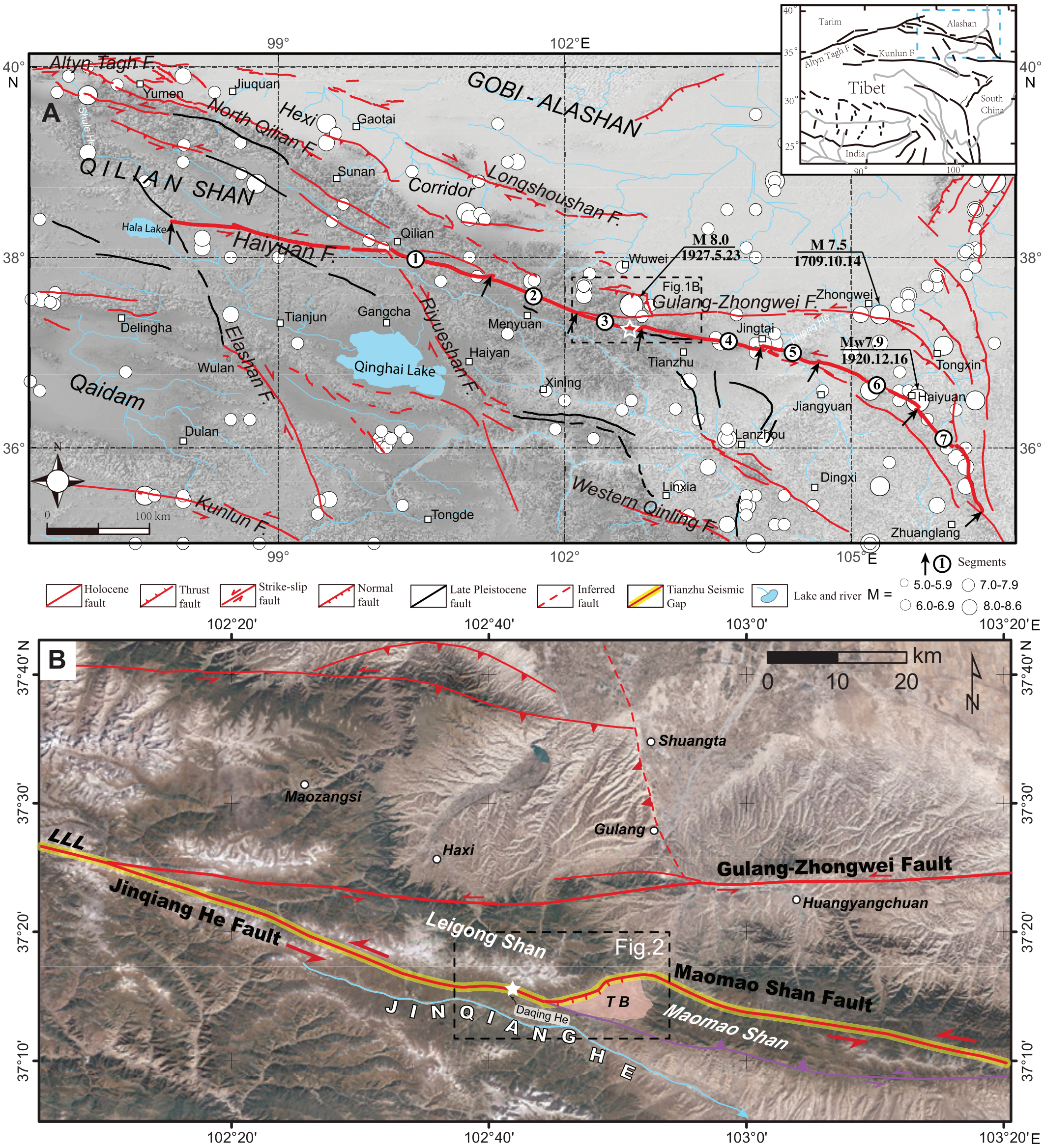

Figure 1. (A) Map of active faults in northeastern Tibetan Plateau, showing seismicity from 780 B.C. to A.D. 2006. Historical earthquakes are from the Division of Earthquake Monitoring and Prediction, State Seismologic Bureau (1995), and instrumental seismicity is from China Earthquake Networks Center (http://www.cenc.ac.cn/). White star indicates study site; dashed box is outline of area in B. F.—fault. Haiyuan fault is subdivided into seven sections separated by black arrows, from west to east: (1) Halahu, (2) Lenglong Ling, (3) Jin Qiang He, (4) Maomao Shan, (5) Jingtai, (6) Haiyuan, and (7) Liupan Shan. Inset is location map showing tectonic framework of the Tibetan Plateau. (B) Active faults along Jin Qiang He section, which extends from Lenglong Ling–Gulang–Jin Qiang (LGH) fault triple junction to the west to Tianzhu pull-apart basin (TB) to the east, left-stepping to Maomao Shan section. Upper Jin Qiang He valley is fed mostly by north-south tributaries flowing down from Leigong Shan to the north and crossing the Haiyuan fault at high angle. LLL—Lenglong Ling.

lower age constraints may be used to bracket the riser age (Mériaux et al., 2005; Cowgill, 2007).

The precision of a late Quaternary slip rate depends upon displacement accumulation and its uncertainty, as well as the reliability of the corresponding dating (Sieh, 1981; Weldon and Sieh, 1985; Van der Woerd et al., 1998, 2006; Cowgill, 2007; Zhang et al., 2007; Cowgill et al., 2009; Gold et al., 2009; Le Béon et al., 2012; Mériaux et al., 2012). Across the Qilian Shan–Hexi Corridor, where extensive loess covers the landscape, optically stimulated luminescence (OSL) or radiocarbon ages of materials collected from within the basal loess provide a minimum date for the end of terrace emplacement (e.g., Li et al., 2009; Jiang et al., 2017; Liu et al., 2018). In this area several studies indicate that loess deposition started just prior to the Holocene (ca. 13–10 ka; Stokes et al., 2003; Küster et al., 2006). Thus, the loess deposition age is a minimum age for the terraces. Because terrace materials capped by loess usually consist of coarse gravels, if one could correct for the shielding effect due to loess cover, in situ cosmogenic nuclides should be an appropriate dating method, ideally complemented by OSL and ^{14}C dating of loess capping materials (e.g., Hetzel et al., 2004, 2019; Le Dortz et al., 2011; Perrineau et al., 2011).

High-resolution topographic data make it possible to image subtle landforms and deformation features due to active tectonics, and to make reproducible and precise measurements, improving understanding of rupture history and slip along faults (e.g., Hudnut et al., 2002; Oskin et al., 2007; Arrowsmith and Zielke, 2009; Zielke et al., 2010, 2015). Satellite or aerial photography offers two-dimensional imagery, which is often used to trace faults and look for offset markers (e.g., Tapponnier and Molnar, 1977; Peltzer et al., 1989; Meyer et al., 1998; Lasserre et al., 1999; Klinger et al., 2011; Middleton et al., 2016). Studies have applied airborne laser scanning (ALS) data to map fault-zone features (e.g., Hudnut et al., 2002; Oskin et al., 2007; Arrowsmith and Zielke, 2009; Liu-Zeng et al., 2013), to survey coseismic surface ruptures (Oskin et al., 2012; Clark et al., 2017; Langridge et al., 2018), and to determine paleo-earthquake slip distributions (Zielke et al., 2010, 2012; Thackray et al., 2013; Chen et al., 2015). Recently, this technique has also been used to measure the most recent rupture traces and offsets along the eastern Haiyuan fault (Chen et al., 2014, 2018; Ren et al., 2016).

Based on new high-resolution topography data and precise dating, we revisited the Daqing site (also named the Sangedun site at 102.7°E in the study of Gaudemer et al., 1995), a location with multiple marker offsets, to reassess the slip rate of the Haiyuan fault. We constrained the slip rate at this site with new offset measurements and a combination of absolute age dating approaches.

GEOLOGIC SETTING

The Haiyuan fault extends for ~1000 km from Hala Hu within the Qilian Shan in the west to the Liupan Shan in the east (Fig. 1; e.g., Tapponnier and Molnar, 1977; Gaudemer et al., 1995). Thermochronological data indicate that the Haiyuan fault initiated along its western section and then propagated eastward to the Liupan Shan area (Zheng et al., 2006; Duvall et al., 2013). The fault is characterized by left-lateral strike slip with oblique-slip components along some strands (Tapponnier and Molnar, 1977; Burchfiel et al., 1989; Gaudemer et al., 1995; Lasserre et al., 1999; Zhang et al., 1988a). Six major 70–300-km-long sections are distinguished and delimited by major step-overs or branches (Fig. 1). Halfway along the Haiyuan fault, a major branch, the Gulang-Zhongwei fault, splays off the Haiyuan fault at the junction of the Lenglong Ling and Jin Qiang He sections. This strand turns back toward the Haiyuan fault east of 106°E in the Liupan Shan section. Large historical earthquakes, such as the A.D. 1709 Zhongwei M 7.5, the A.D. 1920 Haiyuan Mw 7.9, and the A.D. 1927 Gulang M 8.0 earthquakes, have ruptured these two fault sections (Deng et al., 1984; Gaudemer et al., 1995; Ou et al., 2020).

Several field studies along the Haiyuan fault have been carried out during the past 30 yr. For instance, paleoseismic investigations along the Haiyuan (e.g., Zhang et al., 1988b, 2003; Ran et al., 1997; Xiang et al., 1998; Min et al., 2001; Liu-Zeng et al., 2015) and Maomao Shan (e.g., Yuan et al., 1998; Liu-Zeng et al., 2007) sections showed that earthquakes can rupture single or several sections together, and cluster temporally. High-resolution deposition sequences in trenches also provided evidence of magnitude 6–7 earthquakes (Liu-Zeng et al., 2015). Six events are documented on the Lenglong Ling section, the most recent of which may be related to the 1927 Gulang M 8.0 earthquake (Guo et al., 2019; Gaudemer et al., 1995).

Geological slip rates determined along the Haiyuan fault differ greatly, from a few millimeters per year to more than 1 cm/yr. This may be due to different dating approaches and slip reconstruction models applied. For example, Lasserre et al. (2002) proposed a slip rate for the Lenglong Ling segment based on an ~200 m offset of a lateral moraine dated with cosmogenic radionuclides (CRN), yielding a slip rate of 19 ± 5 mm/yr with a lower bound of 11 ± 3 mm/yr. Along the same Lenglong Ling section, He et al. (2000) argued for a lower slip rate of 3.3–4.1 mm/yr based on older OSL dates. Recently, Jiang et al. (2017) estimated a left-lateral slip rate of 6.6 ± 0.3 mm/yr along the eastern section of the Lenglong Ling segment based on late Pleistocene ^{14}C and OSL ages of stream offsets. Along the Maomao Shan segment, Lasserre et al. (1999) determined a slip rate of 12 ± 4 mm/yr, while Yuan et al. (1998) estimated lower slip rates of 4.1–5.4 mm/yr. Yao et al. (2019) recently reassessed the offsets and age control for sites described by Lasserre et al. (1999) and updated the slip rate there to 5–8.9 mm/yr over the late Pleistocene–Holocene. Farther east, the Haiyuan segment, which ruptured in the 1920 Haiyuan earthquake, was assigned a slip rate of 8 ± 2 mm/yr by Zhang et al. (1988b). Li et al. (2009) updated this value to $\sim 4.5 \pm 1$ mm/yr by dating offset alluvial terraces. Combining ^{10}Be CRN ages from surface and subsurface depth profiles in a set of terraces,

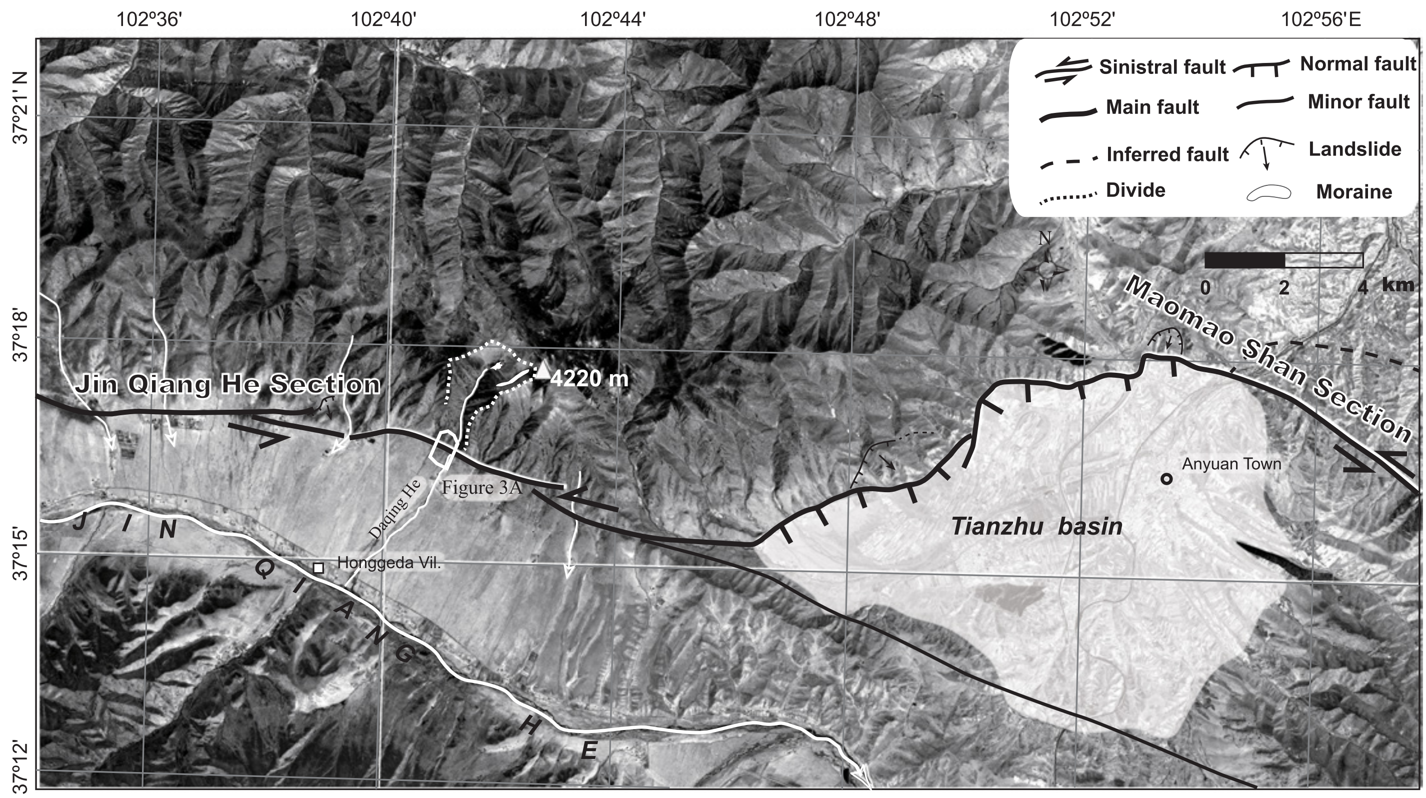

Figure 2. *GF-1* satellite imagery (pixel ~2 m) of Jin Qiang He section of Haiyuan fault near Daqing site (white polygon) upstream from Honggeda village. Light shading delimits Tianzhu half pull-apart basin.

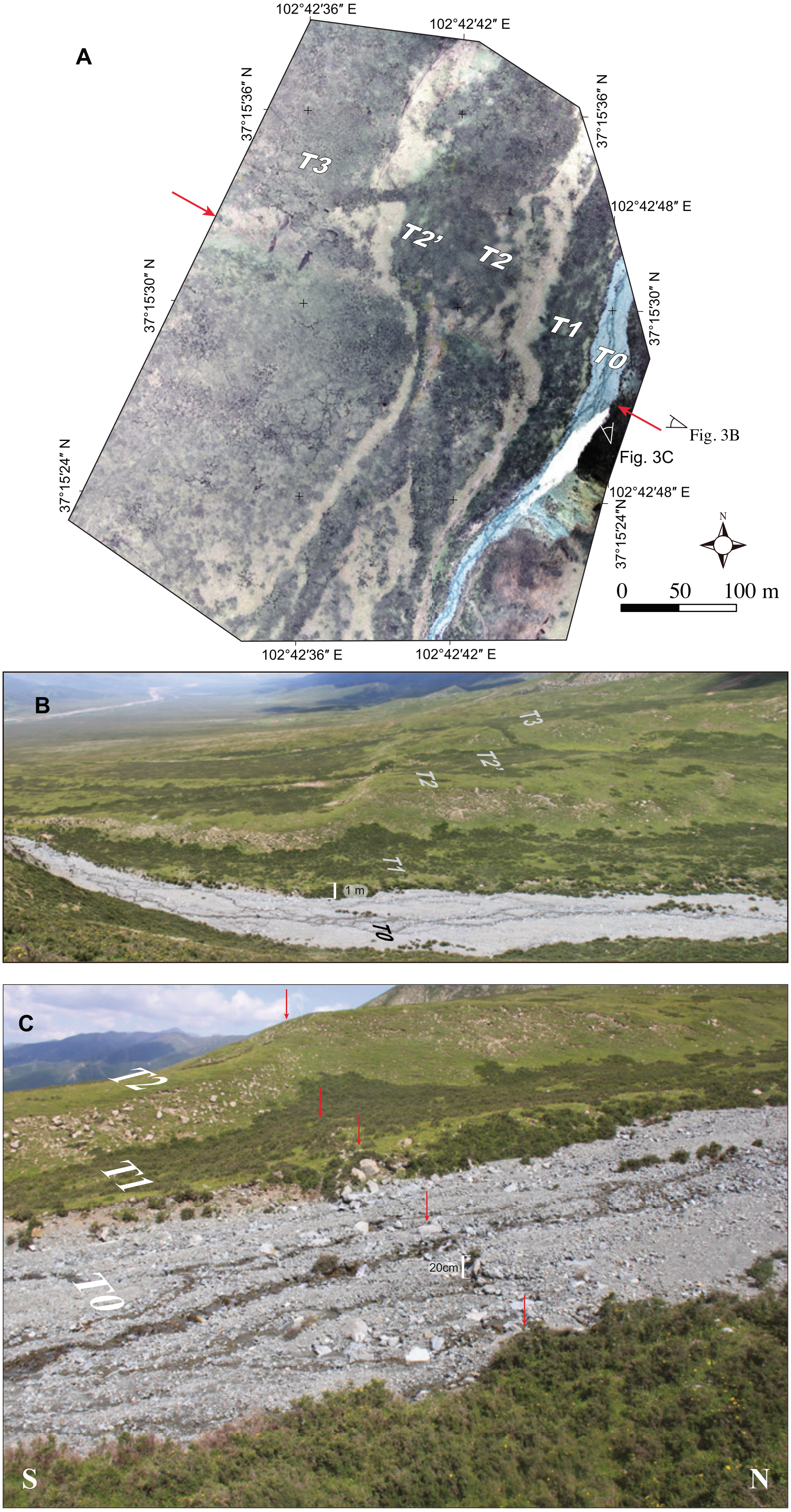

Figure 3. (A) Uncrewed aerial vehicle (UAV)–derived photo mosaic of Daqing site with ~0.2 m resolution. Fault trace is clear across streambed T0 and terraces T1 to T3 to the west. Red arrows point to fault trace. (B) West-looking panoramic field view of faulted terraces at Daqing site. (C) Oblique close-up view showing fault trace across terraces T0 (streambed), T1, and T2.

Matrau et al. (2019) constrained a minimum slip rate of 3.2 ± 0.2 mm/yr along one of the fault strands crossing the Hasi Shan restraining bend, within the western section of the 1920 Haiyuan earthquake rupture.

The Jin Qiang He section (3) and the Maomao Shan section (4) are nearly parallel and linked across a 6-km-wide left step by a N45°E-striking and east-dipping normal fault, which bounds the Tianzhu half-graben or pull-apart basin in the west (Fig. 2; Gaudemer et al., 1995). The Jin Qiang He section fault strikes 110° and offsets alluvial fans and ridges along the northern side of the Jin Qiang He valley. There is no evidence of a large earthquake during at least the past eight centuries along these two fault sections, which are considered together as "the Tianzhu seismic gap" (Gaudemer et al., 1995).

The site of Daqing (or Sangedun site in Gaudemer et al., 1995; Tapponnier et al., 2001b) is located along the eastern part of the Jin Qiang He section, north of the village of Honggeda, and ~80 km east of the sites investigated by Lasserre et al. (2002; see also Fig. 2 here). The mountain range immediately to the north is locally called Leigong Shan, with the highest peak reaching 4326 m above sea level (asl). Traces of the last glaciation, in the form of fresh glacial cirques, are preserved above 3700 m on the southern flank of the mountain range (Gaudemer et al., 1995). Streams incising the steep southern flank of the mountains feed boulder-bearing fluvio-glacial fans that are cut near the apex by the Haiyuan fault. Here, glacial moraines are absent, but to the west in the Lenglong Ling area, glacial landforms are common (Meyer et al., 1998; Lasserre et al., 2002; Owen et al., 2003). OSL and CRN ages of glacial deposits in the Lenglong Ling area indicate that the Last Glacial Maximum (LGM) took place at 21–18 ka, in agreement with the timing of the global LGM (Owen et al., 2003; Wang et al., 2013). Following the cold and arid glacial period, fans and terraces were deposited in the late Pleistocene and early Holocene, due to increased runoff and glacial melting as the climate became warmer (e.g., Meyer et al., 1998; Van der Woerd et al., 2002; Hetzel, 2013). A climatic index analysis at a site on the northern flank of the Leigong Shan suggests that it was warm

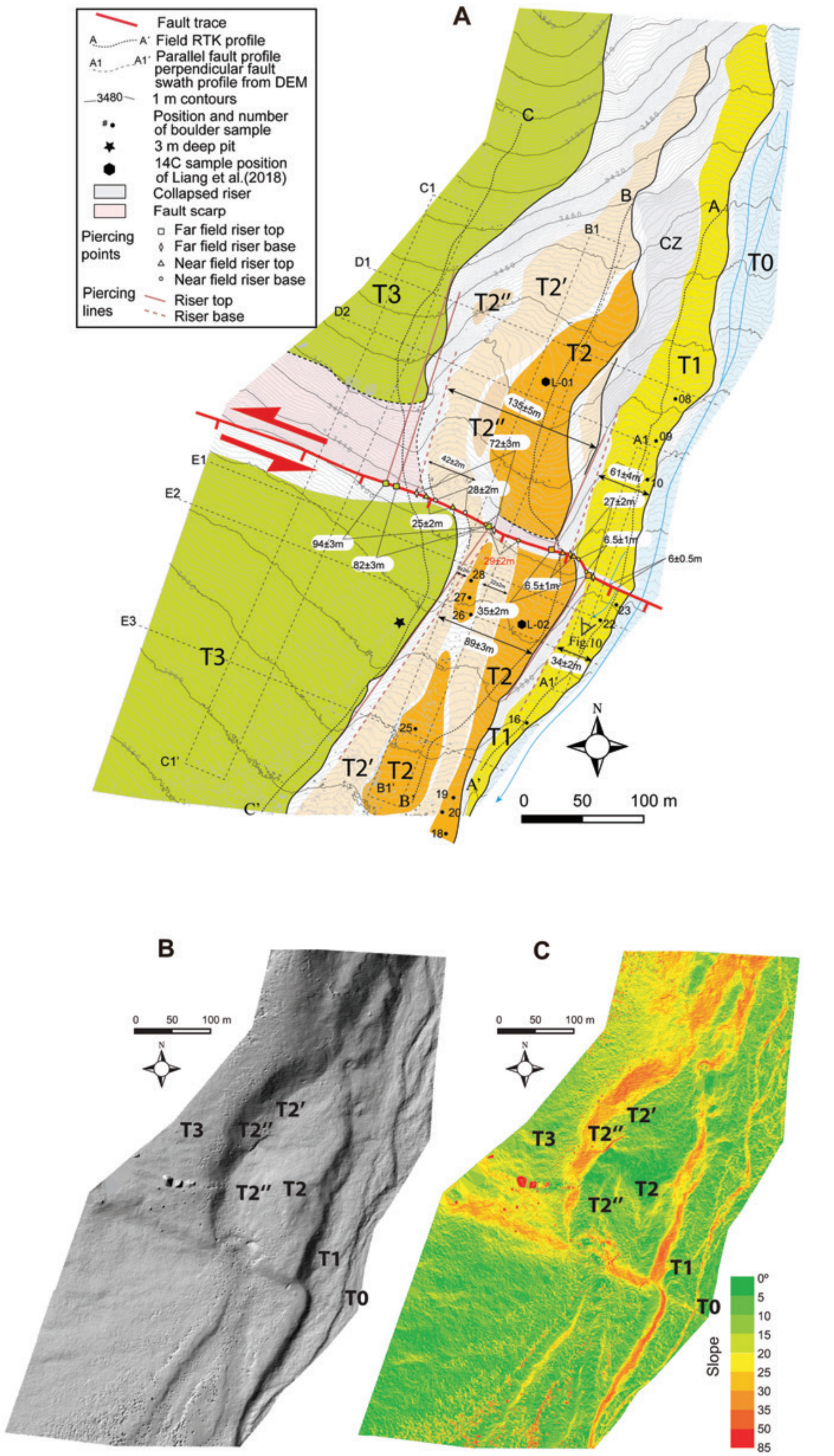

Figure 4. (A) Geomorphic map of Daqing site from field observations, uncrewed aerial vehicle (UAV) photo mosaic interpretation, and high-resolution digital elevation model (DEM) analysis. Contours with 1 m interval were derived from ~0.1-m-resolution terrestrial light detection and ranging (LiDAR) DEM. Dashed lines are topographic profiles shown in Figure 5. Pit and sample positions for dating are indicated. Purple lines are terrace riser piercing lines for horizontal offset measurements. RTK—real-time kinematic global positioning system data. (B) Hillshade and (C) slope map of DEM highlighting terrace surface morphology, distinct terrace risers, and fault scarp.

and wet in the early Holocene (9.6–9.0 k.y. B.P.), and that the most arid period during the Holocene occurred between 9.0 and 8.7 k.y. B.P., when loess was deposited at the site (Wu et al., 1998).

At a regional scale, loess deposits are common but spatially unevenly distributed in the Qilian Shan during the Holocene (Meyer et al., 1998; Küster et al., 2006; Zhang et al., 2015).

At the Daqing site, a stream that flows down from a high catchment (elevation >4000 m asl) and perpendicular to the main fault has abandoned a set of three main terrace levels along its west bank (Fig. 3). Each one of the terraces is offset by the Haiyuan fault. Based on fieldwork, aerial-photo interpretation, and topographic leveling with a theodolite, Gaudemer et al. (1995) determined that the three main terraces are respectively offset horizontally by 143 m, 89 m, and 35 m and vertically by 18 m, 11 m, and 4 m. Assigning an abandonment age of 13.5 ± 2 ka to the highest terrace based on the assumption that it was deposited and abandoned during the wetter and warmer period following the LGM, they proposed a slip rate of 11 ± 4 mm/yr.

LEVELING AND GEOCHRONOLOGY METHODS

We used a combination of terrestrial light detection and ranging (LiDAR), termed TLS herein, uncrewed aerial vehicle (UAV) imagery, and kinematic global positioning system (GPS) data to survey the landforms of the Daqing site. For terrestrial LiDAR, we used a Riegl VZ-1000, with an effective scan range of ~1400 m and a precision of ~5 mm. Three successive scans were needed to cover all the studied area. A Trimble real-time kinematic (RTK) GPS was used to survey the position and elevation of each scanning base. These positions were registered in the different point-cloud data sets together. Because some places could not be scanned by the TLS due to topographic roughness, we used a DJI® Phantom 2 drone equipped with a fixed-focus camera to capture aerial imagery vertically and obliquely to generate an orthophoto mosaic of the site using structure-from-motion (SfM) techniques (Figs. 3 and 4; e.g., James and Robson, 2012; Bemis et al., 2014). The drone took more than

120 photos at a height of ~50 m above the ground surface. The flight paths were parallel to the fault trace with a swath of 30–50 m. We set up six ground control points (GCPs) distributed evenly at the terrace surfaces before collecting photos. The positions of GCPs were also recorded by GPS-RTK. Agisoft® Photoscan was used to process the aerial photos and generate the orthophoto covering the studied site. We projected the digital elevation model (DEM) derived from the TLS point cloud in the same coordinates as the orthophoto mosaic (Figs. 3 and 4). Three topographic profiles were leveled in the field using the Trimble RTK-GPS system described above along the various terrace risers. We also extracted topographic profiles from the high-resolution DEM as single profiles or swath profiles. The profiles were projected either perpendicular or parallel to the fault trace (Figs. 4 and 5).

At the Daqing site, the terrace conglomerates in the piedmont of the Leigong Shan were deposited as debris flows originating from the catchment upslope. The clasts within these conglomerates may have been mobilized from moraines upstream, the remnants of which are still visible in the upper part of the catchment (Fig. 3). Sediments mostly comprise granite, gneiss, and metasedimentary rocks. Large boulders 0.5–2 m in diameter armor the surface of the terraces, and some of them are partially buried due to loess accumulation and soil development. Quartz-rich rock samples for terrestrial CRN dating were collected from the top of boulders using chisel and hammer (Figs. 4 and 6). In addition, a pit was dug into the highest terrace (T3) for subsurface sampling (Figs. 4A and 7). The upper 1.1 m section of the profile consists of an 80-cm-thick dark-brown to black silty soil topping a 30 cm silty (loess) layer mixed with sparse gravels and pebbles less than 1 cm in grain size. In these upper layers, we collected two radiocarbon samples of bulk soil at 62 and 77 cm depths, and two OSL samples at 82 and 104 cm depths (Tables 1 and 2). In the lower conglomeratic part of the profile, we collected eight samples of amalgamated quartz-rich gravels and pebbles (size <5 cm) down to 3 m depth for cosmogenic isotope dating. All sample locations were recorded using a portable GPS, and elevations were adjusted with the topography data from the TLS (Fig. 4; Table 3).

Radiocarbon samples were analyzed by Beta Analytic with accelerator mass spectrometry (AMS; Table 1) and calibrated using Calib 7.1 (Stuiver and Reimer, 1993). The two OSL samples were processed at the Zhejiang Zhongke Institute of Luminescence Testing Technology of China, using methods following Aitken (1998) and Lu et al. (2007). Coarse-grained quartz was purified from samples through chemical separation using 30% H_2O_2, 10% HCl, and 40% HF, and magnetic separation. The ratio of infrared stimulated luminescence (IRSL) to blue light stimulated luminescence (BLSL) was checked to be lower than 45% to make sure the quartz was pure. A Risø TL/OSL-DA-20 reader was used for irradiation, heating, and luminescence measurements (Table 2; Fig. 8). All ages were calculated using a central age model (Galbraith and Roberts, 2012).

The samples analyzed for ^{10}Be cosmogenic nuclides were preprocessed at the Key Laboratory of Crustal Dynamics, China Earthquake Administration. The gravels and pebbles were crushed, and the 250–500 μm fraction was purified with acid leaches to obtain pure quartz; then, hydrofluoric acid was used to dissolve ~30 g of quartz, to which a beryllium-9 carrier solution was added. Beryllium hydroxide ($BeOH_2$) was isolated using cation exchange chromatography, and then it was heated to 700 °C to form beryllium oxide (BeO). Final targets were prepared at the Cosmogenic Isotope Laboratory of the Institut de Physique du Globe de Strasbourg (Centra National de la Recherche Scientifique, University of Strasbourg) and processed at the ASTER-AMS facility of the Centre Européen de Recherche et d'Enseignement des Géosciences de l'Environnement (Aix-en-Provence, France) for measurement (Table 3).

RESULTS

Horizontal and Vertical Cumulative Slip Determination

Combining the DEM with a resolution of ~0.1 m computed from point clouds acquired by TLS, the RTK-GPS topographic profiles, and the aerial orthophoto mosaic acquired by UAV, we produced a geomorphic map of the Daqing site (Fig. 4). Overall, our mapping and leveling are consistent with previous interpretations of the site by Gaudemer et al. (1995). Three main terrace levels are abandoned and preserved on the west bank of the Daqing stream. These are offset both horizontally and vertically due to oblique fault slip. The trace of the main Haiyuan fault can be clearly followed along the steepest part of the topographic scarp trending 110°. The fault trace is also marked by roughly aligned large blocks across the active streambed, as already noted by Gaudemer et al. (1995), which are clearly visible on the aerial photo and in the field (Fig. 3).

The terrace levels are well defined and separated by steep risers (Figs. 4 and 5; Table 4). The terrace surfaces slope southward 14° to 8° from oldest to youngest, reflecting progressive incision and the lower depositional gradient of younger deposits (Figs. 4 and 5). The highest terrace level, T3, is located furthest west of the active riverbed. It is cut and offset by a 15–19-m-high south-facing scarp. The intermediate terrace level is subdivided into older and higher-standing parts, labeled T2, which are characterized by sparse outcropping boulders, inset by 6-m-deep channels, labeled T2′, which are in turn locally inset further by small terrace remnants designated T2″ (Figs. 4 and 5). The lowest terrace level, T1, stands a few meters above the active riverbed. At places, gullying and riser-slope instabilities have added some disturbance to the overall simple geomorphological setting. The height and width of the fault scarp are larger on the older terraces than on the younger ones, due to additional accumulated deformation and progressive degradation of the steep fault scarp (Figs. 3 and 4; e.g., Tapponnier et al., 1990; Zinke et al., 2015). In addition, due to relative vertical motion on the fault, terrace-riser height is larger upstream than downstream, with no significant change in terrace tread average slope (Fig. 5).

Because of lateral stream erosion and local degradation of terrace risers, terrace edges are not linear features, which lends uncertainty to reconstruction of their geometry prior to being offset. Downstream risers T3/T2′ and T2/T1 are curved near the fault trace (Figs. 3 and 4), which suggests that displacement of the risers started to accumulate before the lower terrace levels were completely abandoned. Several studies have addressed the interaction between geomorphic processes and tectonic movement

Figure 5. Topographic profiles across and along terraces at Daqing site. Locations are shown in Figure 4. Gray dots are measurement points; solid black lines along slopes are fitting lines. A-A′, B-B′, and C-C′ are field real-time kinematic global positioning system profiles; others are swath profiles extracted from light detection and ranging (LiDAR) digital elevation model (DEM). Dashed line in swath profiles represents mean elevation value. Small sketch illustrates correction applied to apparent vertical offset of T3 due to oblique orientation of its sloping surface. Vr, corrected vertical offset, is function of Vi (vertical throw measurement from perpendicular fault profile C1-C1′), h is horizontal offset of terrace, and α is angle of terrace slope parallel to fault (in profiles E1, E2, E3; see also Gaudemer et al., 1995).

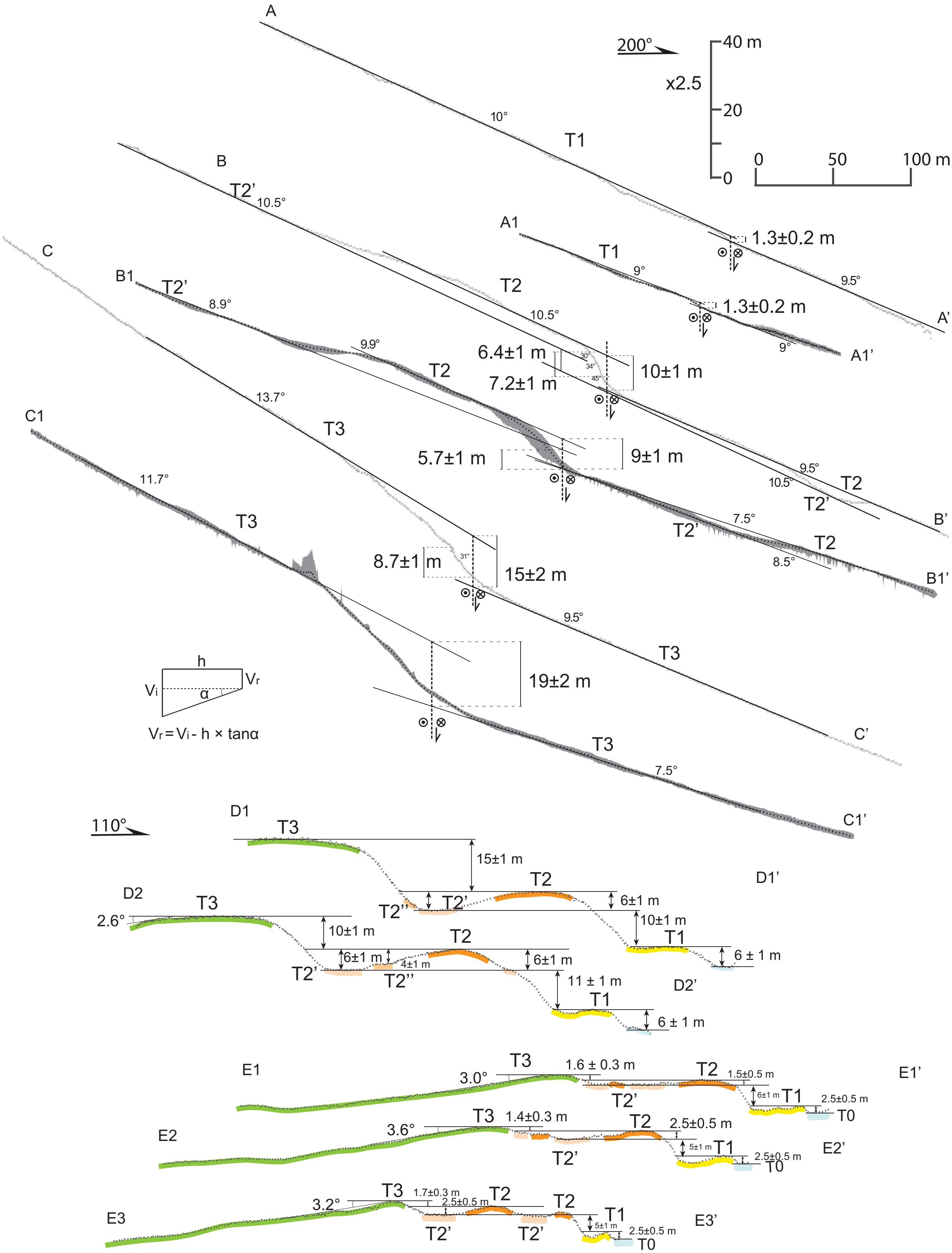

A
A'
A1
A1'
B
B'
B1
B1'
C
C'
C1
C1'
200°
40 m
x2.5
20
0
0
50
100 m
T1
T2
T2'
T3
10°
9°
9.5°
10.5°
8.9°
9.9°
13.7°
11.7°
7.5°
8.5°
1.3±0.2 m
1.3±0.2 m
6.4±1 m
7.2±1 m
10±1 m
5.7±1 m
9±1 m
8.7±1 m
15±2 m
19±2 m
h
Vi
Vr
α
Vr = Vi - h × tanα
110°
D1
D1'
D2
D2'
15±1 m
6±1 m
10±1 m
6 ± 1 m
10±1 m
6±1 m
4±1 m
11 ± 1 m
2.6°
T2''
E1
E1'
E2
E2'
E3
E3'
3.0°
3.6°
3.2°
1.6 ± 0.3 m
1.5±0.5 m
6±1 m
2.5±0.5 m
1.4±0.3 m
5±1 m
1.7±0.3 m
T0

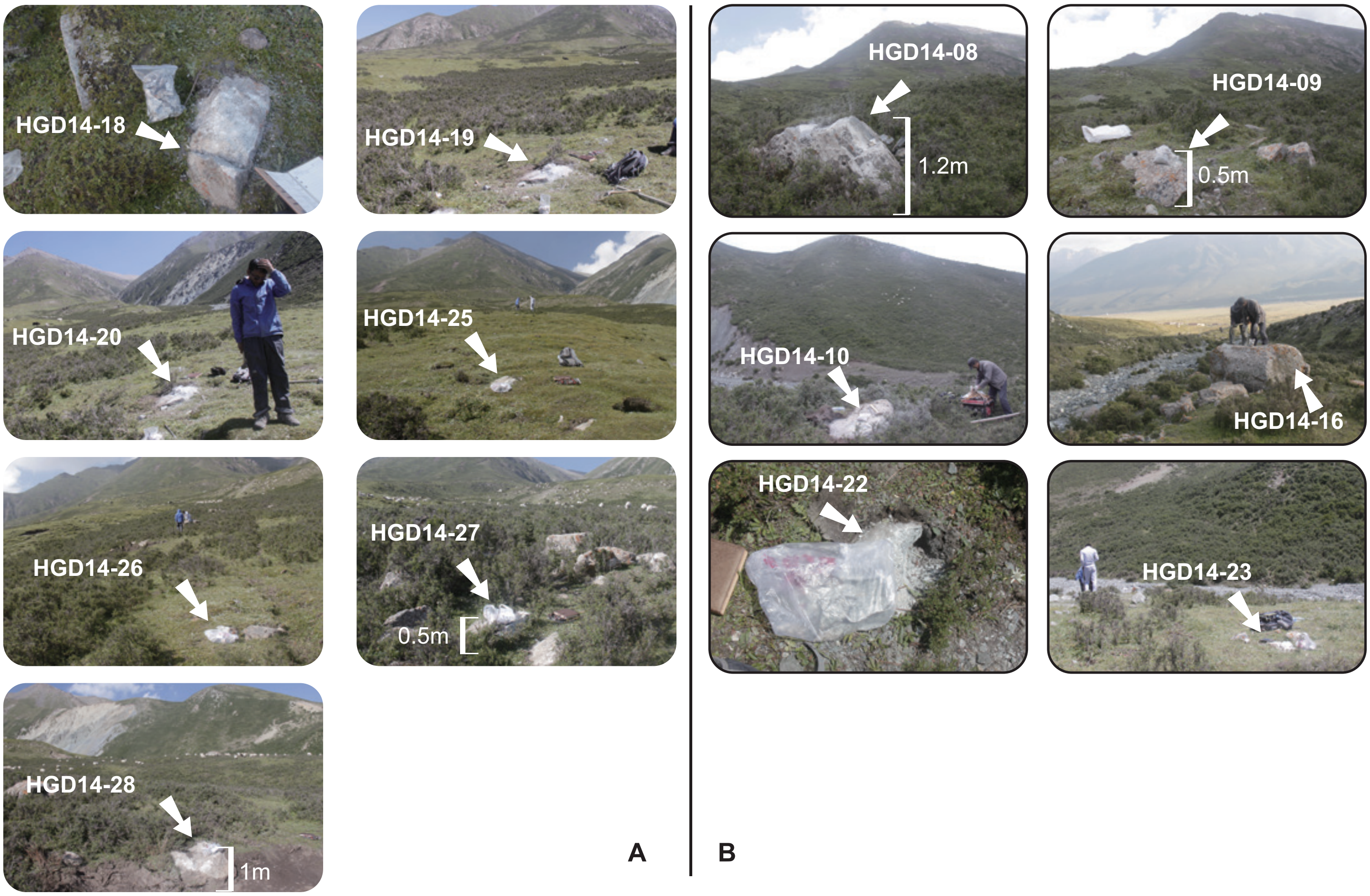

Figure 6. Field photographs of surface boulders sampled for cosmogenic dating from terraces T2 (A) and T1 (B). See positions in Figure 4 and analytical details in Table 3.

to determine whether terrace risers or channel offsets are true tectonic offsets (e.g., Lensen, 1964; Gaudemer et al., 1989; Van der Woerd et al., 2002; Cowgill, 2007; Mériaux et al., 2012; Reitman et al., 2019). To address the difficulty of offset determination from geomorphic features, we thus determined multiple offsets for each riser, using both far- and near-field projections to the fault, and both their top and bottom edges (Fig. 9).

We determined displacement values by fitting far-field riser edges (more than 100 m long and several tens of meters away from the fault trace) and near-field riser edges (a few tens of meters long and close to the fault trace) across the fault. Terrace risers reach up to 20 m height and display slopes of 10°–40°, so that offsets related to riser top and bottom were also specified, especially offsets of curved risers near the fault trace (Figs. 4 and 9; Table 4). It is worth pointing out that the far-field displacements of risers (e.g., D3t, D3b, D2t, and D2b; Fig. 9F) are likely related to the abandonment of the adjacent upper terrace, while near-field displacements (e.g., d3t, d3b, d2t, and d2b; Fig. 9F) are likely related to the adjacent lower terrace.

For the terrace riser top T3/T2′, its upstream nonlinear part may be fit in two ways. Either the piercing line fits tangentially to the two lower convexities to the east or to the higher concavities to the west (Fig. 4A). Downstream, the far-field piercing line is perfectly linear ~60 m away from the fault. Far-field piercing lines of riser base T3/T2′ are almost parallel to the top on both sides of the fault. Correlating riser top piercing lines yielded displacements of 82 ± 3 to 94 ± 3 m (this latter measurement being similar to the 101.5 m of Gaudemer et al., 1995) or, on average, 88 ± 9 m. Piercing lines at the base of the riser constrained an offset of 72 ± 3 m. The near-field riser T3/T2′ is curved both upstream and downstream of the fault. We were able to match riser top (d3t) and base (d3b) with similar values of 25 ± 2 and 28 ± 2 m (Fig. 4; Table 4).

West of T2, the eastern limit of channel T2′, or the base of riser T2/T2′, was only determined in the near field. Its offset of 29 ± 2 m is similar and consistent with d3b (28 ± 2 m) (Fig. 4; Table 4). East of T2, far-field riser top T2/T1 is linear upstream of the fault and ~30 m downstream of the fault. The far-field riser base is almost parallel to the riser top. The offsets of riser T2/T1 top and base are 35 ± 2 m and 27 ± 2 m, respectively, or on average 31 ± 4 m. The near-field riser T2/T1 is curved, particularly downstream of the fault, and its near-field riser top (d2t) and base (d2b) are similarly offset 6.5 ± 1.0 m (d2t and d2b; Fig. 4; Table 4). A small incision in the middle of terrace T1 is also offset by 6.0 ± 0.5 m (Figs. 4 and 10). Near the fault, riser T1/T0 does not preserve lateral slip, even though T1 and T0 have been ruptured in the past, as indicated by the vertical offset of T1 and the visible fault trace across T0 (Figs. 3C and 4). Away from the fault, the far-field riser T1-T0 seems to be left-laterally offset by several meters, although lateral erosion from the active stream cannot be excluded (Figs. 4 and 9).

In summary, both sets of terrace risers, T3-T2′ and T2-T1, show a similar pattern, where the far-field riser top offsets are much larger than the near-field riser base offsets, i.e., 79–97 m versus 23–30 m and 33–37 m versus 5.5–7.5 m

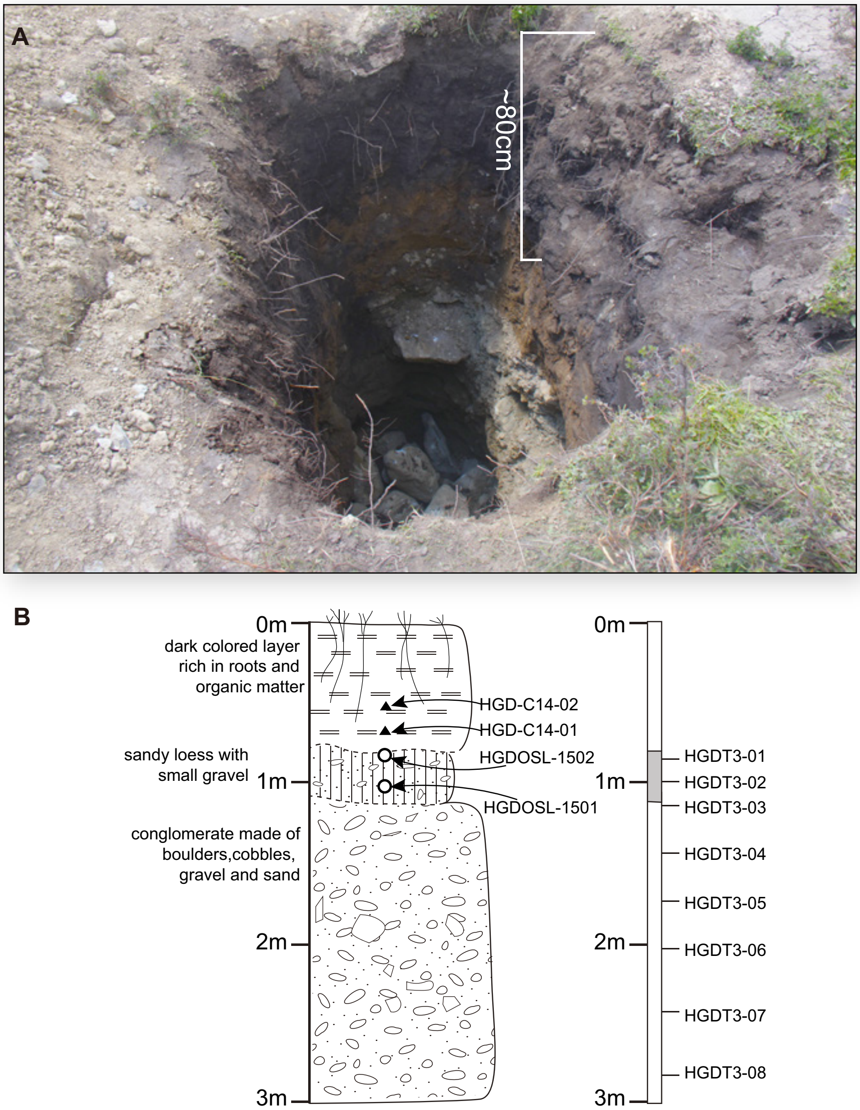

Figure 7. (A) Field view of sampling pit in terrace T3 (see position in Fig. 4). (B) Stratigraphic description of pit. Eight samples of a mix of gravels and pebbles were collected from below 80 cm to 3 m depth for cosmogenic isotope dating (details in Table 3). Open circles are sandy loess samples collected for optically stimulated luminescence dating (Table 2); solid triangles are bulk soil samples for ^{14}C dating (Table 1).

(Fig. 4A). This observation suggests that far-field riser top offset ages are closer to the age of the upper terrace, and that the near-field riser base offset ages are closer to the age of the lower terrace. Therefore, 88 ± 9 m can be defined as a lower bound for the horizontal offset of T3.

TABLE 1. RADIOCARBON ANALYTICAL RESULTS OF SAMPLES FROM TERRACES T3 AND T2, DAQING SITE

Sample	Lab*	Depth (m)	Fraction modern	±	$\delta^{14}C$ (‰)	±	^{14}C age (yr B.P.)	±	2σ calibrated age† (yr B.P.)
HGD-C14-01	414950	0.77	0.4236	0.0016	–576.4	1.6	6900	30	7790–7675
HGD-C14-02	414951	0.62	0.4414	0.0016	–558.6	1.6	6570	30	7555–7545
L-01§		0.89					8630	90	9900–9474
L-02§		0.82					8180	140	9475–8715

*All samples were dated by accelerator mass spectrometry at Beta Analytic.
†Calibration with Calib 7.1 (Stuiver and Reimer, 1993) did not include probability distribution of range <0.1.
§L-01 and L-02 are from Liang et al. (2018), and fraction modern and $\delta^{14}C$ information is not known.

The bounds of the offset of T2 range between 72 ± 3 m and 35 ± 2 m, but the actual value is probably closer to the upper bound because the channel T2′ offset is well constrained at 28–29 ± 2 m. Finally, the offset of T1 is well constrained at 6–6.5 ± 1 m from the similar values of the near-field riser base offset and the incision across T1 (Table 4).

In addition to left-lateral horizontal slip, the Haiyuan fault exhibits a vertical component of slip at this site (Figs. 3, 4, and 5). The scarp height measured along swath profile C1-C1′ in the middle of terrace T3 (19 ± 2 m) is larger than the height from profile C-C′ following the offset terrace edge (15 ± 2 m; Figs. 4 and 5). This discrepancy is due to lateral displacement of the obliquely sloping terrace T3 relative to the fault trace (e.g., Peltzer et al., 1988; Gaudemer et al., 1995; Rodgers and Little, 2006; Chevalier et al., 2016). Correcting the measured offset of 19 ± 2 m (Vi) by taking into account the slope of terrace T3 (on average 3.1° to the west in a direction parallel to the 110° strike of the fault; see profiles D2 and E1–E3 in Fig. 5) and a horizontal offset of 88 m yields a corrected vertical offset of 14 ± 2 m (Vr) similar to the value of 15 ± 2 m from the offset riser top. Maximum slopes of terrace T2 on both sides of the fault are similar and oriented perpendicular to fault trace, so that no correction is needed for T2, and its vertical throw is 10 ± 1 m (Fig. 5; Table 4). The terrace level T2′ slopes on average perpendicular to the fault trace, and its vertical offset ranges from 5.7 ± 1.0 m (profile B1-B1′) to 6.4 ± 1.0 m (profile B-B′), thus on average 6.0 ± 1.5 m (Fig. 5; Table 4). The slopes of T1 are similar upstream and downstream, and the height of the fault scarp across T1 is 1.3 ± 0.2 m (Fig. 5).

To summarize, the four terraces T3, T2, T2′, and T1 at the Daqing site have horizontal and vertical offsets of 88 ± 9 m, 33–75 m, 28.5 ± 2.0 m, and 6.5 ± 1.0 m and 15 ± 2 m, 10 ± 1 m, 6.0 ± 1.5 m, and 1.3 ± 0.2 m, respectively (Table 5). These values display a consistent vertical to horizontal ratio that ranges from 0.170 to 0.211 (average 0.191 ± 0.018; Table 5), testifying to a constant slip vector overall (Fig. 11).

Terrace Ages

To constrain the age of abandonment of T3, we dug a 3-m-deep pit in the downstream tread of terrace T3 (Figs. 4A and 7). The upper 1.1 m section of the profile exhibits a 30 cm sandy-loessic layer overlain by an 80-cm-thick dark-brown silty soil, which partly developed by incorporating wind-blown loess and sand. Below 1.1 m depth, the profile penetrates the conglomeratic terrace deposit consisting of boulders, cobbles, gravels, and sand. Two

TABLE 2. ANALYTICAL RESULTS OF OPTICALLY STIMULATED LUMINESCENCE (OSL) SAMPLES FROM TERRACE T3, DAQING SITE

Sample no.	Lab. no*	Depth (m)	Water content† (%)	U§ (ppm)	Th§ (ppm)	K§ (%)	Cosmic dose rate (Gy/k.y.)	Grain size (μm)	Dose rate (Gy/k.y.)	Equivalent dose# (Gy)	Age** (ka)
HGDOSL-1502	15–64	0.82	2.6	2.71 ± 0.1	14.4 ± 0.39	2.18 ± 0.06	0.32 ± 0.02	90–125	4.06 ± 0.15	35.3 ± 1.3	8.7 ± 0.5
HGDOSL-1501	15–63	1.04	8.04	2.45 ± 0.1	12.8 ± 0.36	2.12 ± 0.06	0.31 ± 0.02	90–125	3.61 ± 0.13	44.2 ± 0.8	12.2 ± 0.5

*All samples were processed at Zhejiang Zhongke Institute of Luminescence Testing Technology.
†Measured water content.
§Concentrations of U, Th, and K were measured by neutron activation analysis at the China Institute of Atomic Energy.
#All equivalent dose values conform to normal distribution.
**Calculated with the central age model (Galbraith and Roberts, 2012).

OSL samples from the loess layer yielded ages of 12.2 and 8.7 ka in stratigraphic order (Fig. 7; Table 2). Two radiocarbon samples from the lower part of the soil yielded ages of 7.7 and 7.6 ka, also in stratigraphic order (Fig. 7; Table 1). Whether the loessic layer is of eolian origin or reworked loess in overbank deposits cannot be confirmed. In any case, the 1.1-m-thick top layer of the terrace indicates deposition processes incompatible with the presence of an active stream, and thus it indicates that the underlying conglomerate had been abandoned prior to deposition of these upper layers, i.e., prior to 12.2 ka. To better constrain the age of abandonment of the terrace, we modeled the ^{10}Be concentration with depth for eight amalgamated samples of gravel and pebbles collected from the conglomeratic terrace deposit (Fig. 7; Table 3). To take into account the shielding effect of the loess and soil, we propose three end-member models (Fig. 12A). The first one (model 1) is a maximum-shielding or maximum-age model, for which, despite knowledge of the loess and soil ages from other methods (OSL and ^{14}C), we consider that loess and soil were deposited immediately after the abandonment of the conglomerate forming T3 (Fig. 12A). Considering the respective density of 2.0 g/cm^3 for sandy-loess and of 1.2 g/cm^3 for soil, the best fit of the ^{10}Be data is obtained with an exposure age of 21.6 ± 4.6 ka (t_{1-1}) (Fig. 12D). Clearly, given the age of the lowermost OSL sample of 12.2 ka, this age is not realistic and implies stepwise or progressive emplacement of the sandy-loess and soil layers, which we considered in the subsequent models. A second model (model 2) considers the oldest ages of the sandy-loess and soil deposit as the moment when these layers were deposited (Fig. 12B). This model has thus three exposure phases, a first one corresponding to the abandonment of the conglomerate without shielding (between t_{2-1} and t_{2-2}); a second one with 30 cm of sandy-loess shielding starting at 12.2 ka (t_{2-2}); and a third one with the additional 80 cm of soil shielding starting at 7.7 ka (t_{2-3}). The sandy-loess and soil layers are assumed to have been deposited instantaneously. Model 2 gives a time of exposure of the conglomerate without shielding of 2.7 ka and thus an abandonment age of 14.9 ka (t_{2-1}) (Fig. 12E). The third model (model 3) is similar to model 2 but instead of assuming instantaneous deposition of the sandy-loess and soil layers, it considers progressive deposition of the shielding layers: 30 cm of loess deposited between 12.2 ka and 7.6 ka (6.5 cm/k.y.) and 80 cm of soil deposited between 7.6 ka until today (10.5 cm/k.y.) (Fig. 12C). Model 3 is a minimum shielding model or minimum-age model and gives an abandonment age of 13.7 ka (t_{3-1}). The result of the third model is compatible with all age data, and we thus suggest an abandonment age for terrace T3 of 13.7 ± 1.5 ka (Fig. 12F).

For terraces T2 and T1, we collected samples made of pieces of the top of the large, 0.8–2-m-diameter, well-embedded boulders (Figs. 4 and 6; Table 3). As visible on the field views in Figure 6, the boulders are variable in size, in height above soil surface, and also in overall shape, ranging from well rounded to angular. Despite inspection of the boulders, it could not be ascertained if they have or have not experienced alteration or spallation. We sampled a total of 13 boulders and selected the best-preserved parts at their tops (Fig. 6; Table 3). Seven samples were collected on terrace T2 south of the fault, and six samples were collected on terrace T1, three to the north and three to the south of the fault (Fig. 4; Table 3). Both ^{10}Be concentration distributions of the samples collected on T2 and T1 show significant scatter in the data, with overlapping values between terraces (Fig. 13A). This scatter may be related to unevenly distributed and large inheritance among the boulders and/or variable erosion affecting the protruding large boulders at the surface of the terraces (e.g., Ritz et al., 2006; Ryerson et al., 2006; Le Dortz et al., 2011, 2012). Such ^{10}Be concentration scatter is a common feature of boulders originating from small-size high-mountain glacial catchments where accumulation and transport vary with climate changes (e.g., Putkonen and Swanson, 2003; Heimsath and McGlynn, 2008; Heyman et al., 2011). Boulders may have sat at various depths in moraines upstream at high elevation during a large part of the Pleistocene before being transported episodically, due to increased moist periods and during brief flash floods. Unlike large catchments with deep valley fill, most of the conglomerate-forming parts of fans and terraces at the outlet of the upper valley across the fault zone were probably never buried deep enough to be shielded completely from cosmic rays. The deepest gravels in the T3 depth profile have concentrations representing ~20%–30% of the surface samples, which represent a significant amount of inherited ^{10}Be acquired upstream. This amount of inheritance may be indicative of the intermittent stream dynamics and evidence of sediment accumulation in the catchment. Inheritance may be distributed differently in amalgamated gravels and large boulders, as their mode of transport and residence time in the catchment differ greatly (e.g., Benedetti and Van der Woerd, 2014; Carretier et al., 2015). Assuming that the scatter in ^{10}Be concentration is due to inheritance, boulders with minimal inheritance may be closer to the true surface age, rather than the typical assumption of the geometric mean as representative of exposure age (e.g., Le Dortz et al., 2011; Owen et al., 2011; Prush and Oskin, 2020). We modeled the T1 and T2 surface clast data sets using the inheritance model of Prush and Oskin (2020) (Fig. 13B). For terrace T2, the inheritance model returned an exposure age of 14.4 $^{+1.6}/_{-3.0}$ ka, overlapping the age of the youngest sample, 13.4 ± 1.3 ka (sample HGD14-27; Fig. 13A; Table 3). This age is also within error of the age of the upper terrace T3 (13.7 ± 1.5 ka), suggesting rapid abandonment of these treads. Additional age constraints for T2 are given by radiocarbon dates of the overlying soil from the study of Liang et al. (2018). The ages obtained in two pits in the top soil of terrace T2 upstream and downstream of the fault indicate that T2 must have been abandoned before 9.3 ± 0.6 ka (Fig. 4; Table 1), consistent with the ^{10}Be surface clast data set. Thus, we define the minimum age of terrace T2 at 9.3 ± 0.6 ka.

For terrace T1, the scatter in ^{10}Be data from the six surface samples is similar to terrace T2. The inheritance model returned a T1 exposure age that is effectively modern (Fig. 13B).

TABLE 3. ^{10}Be ANALYTICAL DATA AT DAQING SITE

Samples	Mass quartz (g)	Total ^{9}Be (mg)	Latitude (°N)	Longitude (°E)	Altitude (m asl)	Sample depth* (cm)	Sample thickness (cm)	Shielding factor†	Sample type	Sample size§	^{10}Be/^{9}Be AMS ratio# (10^{-13})	^{10}Be/^{9}Be AMS error** (%)	[^{10}Be] (at/g quartz)††	Exposure age§§ (yr)
Terrace T1										H/L (m)				
HGD14-08	30.107	0.2461	37.259544	102.696663	3441	0	2.5	0.9911	Granite boulder	1.2/2	11.0676	3.1680	607661 ± 22800	15081 ± 1483
HGD14-09	26.9599	0.2699	37.259254	102.696609	3432	0	2.5	0.9911	Granite boulder	0.5/1.3	5.1828	3.0904	350537 ± 12920	8789 ± 861
HGD14-10	25.7075	0.2410	37.259041	102.696503	3426	0	2.5	0.9911	Gneiss boulder	1/1.5	7.5601	3.1744	477175 ± 17931	12013 ± 1181
HGD14-16	30.0079	0.2458	37.256313	102.695001	3369	0	2.5	0.9911	Granite boulder	1.6/3.5	3.0252	3.1761	165590 ± 6224	4456 ± 437
HGD14-22	29.8354	0.2500	37.256969	102.695702	3389	0	2.5	0.9911	Granite boulder	0.1/0.8	6.7183	3.1746	379378 ± 14255	9764 ± 959
HGD14-23	29.972	0.2517	37.257381	102.695984	3393	0	2.5	0.9911	Granite boulder	0.2/1.2	0.8057	3.5217	48415 ± 1963	1317 ± 131
Terrace T2														
HGD14-18	30.0132	0.2901	37.255253	102.694336	3351	0	2.5	0.9925	Granite boulder	0.2/0.8	2.9682	3.0821	720220 ± 26491	18540 ± 1820
HGD14-19	24.5073	0.2253	37.255444	102.69445	3354	0	2.5	0.9925	Granite boulder	0.2/1.1	14.1264	3.4983	871322 ± 35165	22163 ± 2209
HGD14-20	30.0075	0.2495	*2 m south of sample 19*			0	2.5	0.9925	Granite boulder	0.2/1.1	27.9118	1.9939	1553981 ± 43997	37612 ± 3601
HGD14-25	30.0081	0.2555	37.256226	102.694389	3371	0	2.5	0.9925	Granite boulder	0.2/1	13.6706	3.0506	781051 ± 28532	19812 ± 1944
HGD14-26	25.0845	0.2432	37.257112	102.69458	3388	0	2.5	0.9925	Granite boulder	0.1/1.3	12.3173	3.0546	801699 ± 29317	20124 ± 1975
HGD14-27	30.0488	0.2546	37.257439	102.694618	3391	0	2.5	0.9925	Granite boulder	0.5/1.5	9.1587	3.1078	521787 ± 19311	13360 ± 1311
HGD14-28	30.0016	0.2530	37.257252	102.69455	3393	0	2.5	0.9925	Gneiss boulder	1/1.5	11.2099	3.1186	634911 ± 23556	16098 ± 1581
Terrace T3 depth profile										(cm)				
HGDT3-01	31.4296	0.2592	37.257061	102.693886	3389	85	5	0.9936	Gravels, pebbles	<5	12.9533	2.4296	716994 ± 22605	*see model*
HGDT3-02	29.9764	0.2484			3389	100	5		Gravels, pebbles	<5	20.4441	2.6603	1135218 ± 37852	/
HGDT3-03	25.1784	0.2563			3389	115	5		Gravels, pebbles	<5	8.6821	3.1803	594458 ± 22363	/
HGDT3-04	32.0859	0.2514			3389	145	5		Gravels, pebbles	<5	7.6592	3.2954	404008 ± 15594	/
HGDT3-05	30.1135	0.2566			3389	175	5		Gravels, pebbles	<5	5.7488	3.0688	330590 ± 12127	/
HGDT3-06	29.3054	0.2540			3389	205	5		Gravels, pebbles	<5	6.1867	3.0946	361628 ± 13344	/
HGDT3-07	30.0178	0.2501			3389	245	5		Gravels, pebbles	<5	6.9217	3.5702	388547 ± 15919	/
HGDT3-08	30.041	0.2549			3389	285	5		Gravels, pebbles	<5	4.5729	3.2264	262522 ± 9979	/

Note: All samples were processed at the Key Laboratory of Crustal Dynamics, China Earthquake Administration.

*Depth measured from present-day loess-covered surface.

†Determined with CRONUS online calculator (Balco etal., 2008).

§H—height of boulder above ground, L—longest boulder dimension. Size of pebbles and gravels in depth profile were less than 5 cm.

#Accelerator mass spectrometry (AMS) measurements were performed at ASTER in the Centre de Recherche et d'Enseignement de Géosciences de l'Environnement (CEREGE), Aix-en-Provence, France. Data were normalized with standard Cerege STD (Braucher etal., 2015) with a ^{10}Be/^{9}Be ratio of (1.191 ± 1.09) × 10^{-11}, and corrected with analytical blank ratio of 5.7064 × 10^{-15}.

**AMS error only.

††Error is quadratic sum of AMS and weighing errors, in addition to a 2% uncertainty on ^{9}Be carrier concentration.

§§0 erosion/0 inheritance exposure age was calculated with the CRONUS 2.3 calculator (Balco etal., 2008; http://hess.ess.washington.edu/), with time-dependent Lal (1991)/Stone (2000) scaling scheme for spallation. Sea-level high-latitude production rate of 4.00 atoms/(g quartz)/yr (Borchers etal., 2016) and ^{10}Be half-life of 1.387 m.y. (Korschinek etal., 2010; Chmeleff etal., 2010) were used, with rock density set to 2.7 g/cm^3. Error is external uncertainty.

However, due to the limited number of measurements, it is unlikely that the inheritance was uniformly sampled, limiting confidence in the model age (Prush and Oskin, 2020). In the absence of additional age constraints, we assume that the age of terrace T1 is no older than its youngest sample, HGD14-23, i.e., 1.3 ± 0.1 ka (Fig. 13A; Table 3).

Slip Rate

All slip rates were calculated with one sigma precision assuming Gaussian age and offset distributions, or boxcar distributions when bounds of the age or offset were estimated, like, for instance, for terrace T2 (Table 5; e.g., Daëron et al., 2004; Zechar and Frankel, 2009). Dividing the lower bound of the cumulative displacement of terrace T3, defined by the terrace T3/T2′ riser top offset of 88 ± 9 m, by the abandonment age of T3 of 13.7 ± 1.5 ka yielded a minimum left-lateral slip rate of 6.4 ± 1.0 mm/yr. The bounds of the offset of terrace T2 of 72 ± 3 m and 35 ± 2 m accumulated after 9.3 ± 0.6 ka yielded a rate of 5.8 ± 1.6 mm/yr. The T2′ channel offset of 28.5 ± 2 m remained undated in the absence of ages for T2′. Taking the age of 1.3 ± 0.1 ka estimated for terrace T1 and its 6.5 ± 1 m offset yielded a slip rate of 5.0 ± 0.9 mm/yr. This latter rate should be considered with caution, because the 6.5 m offset may be interpreted as resulting from slip in a single event, and the lower slip-rate value may indicate that the next large seismic event is overdue (Fig. 14; Table 5).

Using the observation of a near-constant slip vector at the Daqing site (Fig. 11) and the better-determined vertical offset of the terraces (Table 5), we may estimate the age of terrace T2′ from its vertical offset of 6.0 ± 1.5 m and the age of T3, yielding 5.4 ± 1.0 ka. Similarly, the age of T1, vertically offset by 1.3 ± 0.2 m, may be estimated to 1.2 ± 0.2 ka, concordant with our assumption that it may be dated with the youngest surface boulder age (1.3 ± 0.1 ka; Table 3). The same relations may be used to further constrain the loosely determined horizontal offset of terrace T2, which is thus likely offset ~51 m, an offset not preserved at the Daqing site, probably due to lateral erosion during incision.

DISCUSSION AND IMPLICATIONS

Diachronous Riser Formation

The geologic slip rate reflects faulting behavior over the long term. Geologic rates are a basic datum for understanding strain accommodation through a system of faults and also one of the most important indicators for the earthquake

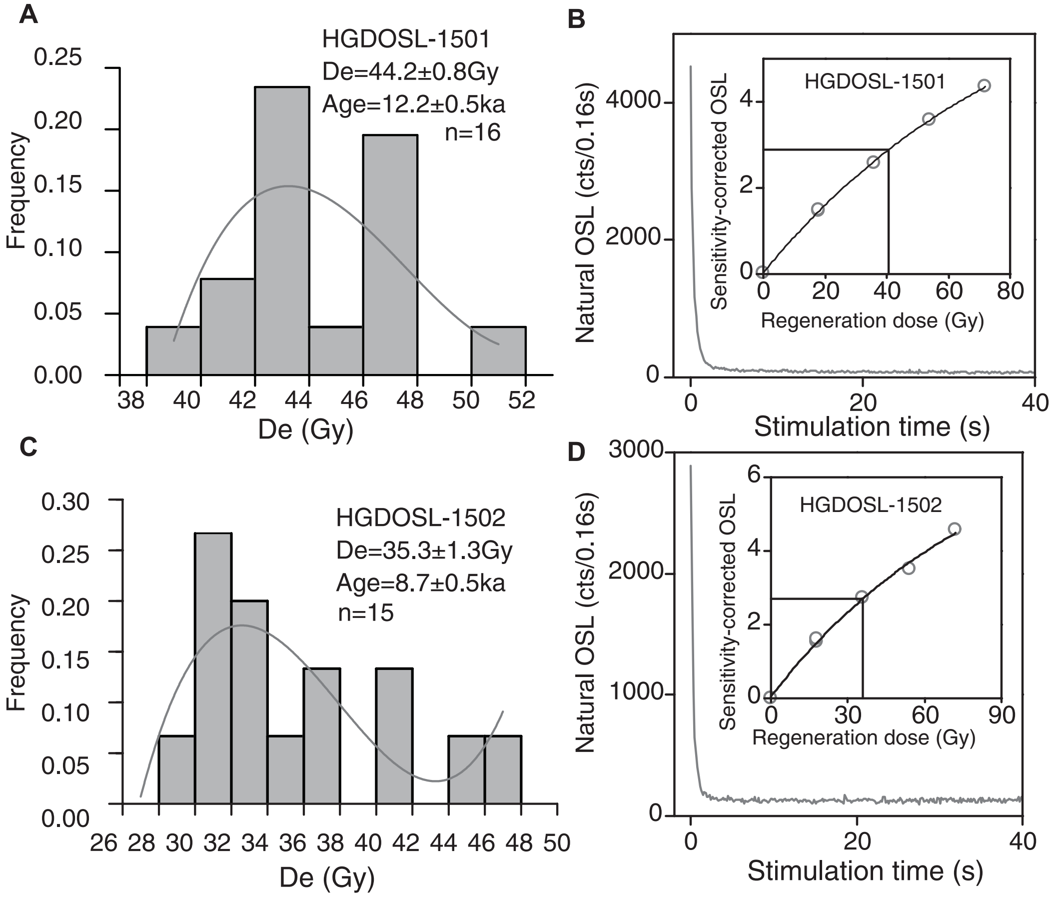

Figure 8. Equivalent dose (De) distributions, natural optically stimulated luminescence (OSL) decay curve, and growth curves for samples HGDOSL-1501 (A, B) and HGDOSL-1502 (C, D), respectively.

potential of a fault. Considerable efforts have been devoted to determining the slip rate on active faults in and around the Tibetan Plateau. Although determination of a geologic fault slip rate is simple in principle, it is subject to considerable uncertainty. The difficulty lies in the fact that the duration of offset accumulation is often approximated by a surrogate age. Indeed, terrace risers are commonly used as offset features in slip-rate determination of faults in northern Tibet, including the Haiyuan, the Altyn Tagh, and the Kunlun faults (e.g., Peltzer et al., 1989; Meyer et al., 1996; Van der Woerd et al., 1998, 2000, 2002; Lasserre et al., 1999; Mériaux et al., 2004, 2005, 2012; Kirby et al., 2007; Cowgill, 2007; Cowgill et al., 2009). These are erosive features, which likely form diachronously, starting to record offset after the abandonment of the upper terrace and sometimes before the abandonment of the lower terrace (e.g., Ryerson et al., 2006; Harkins and Kirby, 2008; Gold et al., 2009; Mériaux et al., 2012). For a given terrace riser offset, the abandonment age of the upper terrace surface provides the maximum age of slip accumulation, and thus the lower bound of the true slip rate. Accordingly, the lower terrace surface age represents the minimum age of slip accumulation and thus the upper bound of the slip rate.

Terrace riser preservation results from the interaction between river erosion and displacement by the fault. In general, a terrace riser on the left bank of a river crossing a left-lateral fault is protected; i.e., continuous left-lateral slip moves the downstream section of the riser away from the stream center, and it is less frequently refreshed and thus more likely to record offset before the abandonment of the lower terrace (e.g., Cowgill, 2007). On the contrary, left-lateral slip on the fault moves the downstream part of the right-bank riser toward the center and in alignment with the upstream channel. This configuration favors more frequent riser refreshment and obliteration of offset before the abandonment of the lower terrace (e.g., Van der Woerd et al., 1998; Tapponnier et al., 2001a, 2001b). However, our investigation at the Daqing site shows incomplete riser refreshment and slip accumulation before the lower terrace was abandoned. Our mapping and offset measurements of the sequentially abandoned terrace surfaces suggest that the right-bank terrace risers, i.e., erosive side, were subject to incomplete riser refreshment and partial preservation of riser offset. Several reasons may explain this situation at the Daqing site. First, the obliquity in slip vector and the accumulation of vertical displacement on the fault would induce more incision in the upstream parts of the terraces (Figs. 4 and 5), increasing channelization upstream and possibly less erosion downstream. Second, the main river trunk may have reduced its width progressively with time and remained channeled on the eastern side of the terraces, thus favoring preservation of the accumulated offsets.

Upper and Lower Bounds of the Slip Rate

The differences between geological slip rates from previous studies along the Haiyuan fault stem mainly from this uncertainty of using upper terrace surface versus lower terrace surface ages as the surrogate for the true offset age of the terrace riser. For example, Lasserre et al. (1999) reported a rate of 12 ± 4 mm/yr on the eastern Maomao Shan

TABLE 4. TERRACE GEOMETRY, VERTICAL TERRACE OFFSETS, AND HORIZONTAL TERRACE RISER OFFSETS

Marker	Parameter	Value (m)	Error (m)	Note
Tread widths				
T1 upstream	W1u	61	4	
T1 downstream	W1l	34	2	
T2′ upstream		42	2	
T2′ downstream west		9	2	
T2′ downstream east		22	2	
T2 tread	W2u	135	5	
T2 tread	W2l	89	3	
Riser heights				
T1-T0	R1u	6	1	Upstream
	R1d	2.5	0.5	Downstream
T2′-T1		10–11	1	Upstream
		5–6	1	Downstream
T2″-T2′		2	1	Upstream
T2-T2′		6	1	Upstream
		1.5–2.5	0.5	Downstream
T2-T1	R2u	16–17	1	
	R2d	7.5	1	Downstream
T3-T2′		16–21	1	Upstream
		3.1–4.2	0.5	Downstream
T3-T2	R3u	10–15	1	Upstream
	R3d	1.4–1.7	0.3	Downstream
Vertical terrace offsets				
T1 A-A′	Sc1	1.3	0.2	Slope 10°/9.5°
T1 A1-A1′		1.3	0.2	Slope 9°/9°
T2′ B1-B1′		5.7	1	Slope 8.9°/8.5°
T2′ B-B′		6.4	1	Slope 10.5°/10.5°
T2 B1-B1′	Sc2	9	1	Slope 9.9°/7.5°
T2 B-B′		10	1	Slope 10.5°/9.5°
T3 C1-C1′	Sc3	19	2	Slope 11.7°/7.5°
T3 C-C′		15	2	Slope 13.7°/9.5°
Horizontal riser offsets				
Stream	Ds	6.0	0.5	
T2/T1	D2t	35	2	
	D2b	27	2	
	d2t	6.5	1	
	d2b	6.5	1	
T3/T2	D3t	94	3	
		82	3	
	D3b	72	3	
	d3t	25	2	
	d3b	28	2	
T2′	d2′b	29	2	
	West bank	28	2	

section of the Haiyuan fault using the lower terrace age, i.e., the minimum age for offset accumulation, and thus this is an upper bound for the true slip rate. Conversely, much lower reported slip rates, such as 3.1–5.8 mm/yr on the Laohu Shan section (Yuan et al., 1998; Liu et al., 2018), were based on the upper terrace surface age for slip accumulation, and thus they provide a lower bound for the true slip rate. As the many slip-rate studies of the Haiyuan fault show, those finding a rate of ≤5 mm/yr are mainly based on an upper terrace reconstruction. In only a few cases, both the upper and lower terraces were dated (Li et al., 2009; Zheng et al., 2013). If the lower terrace reconstruction scenario is considered in these studies, an upper bound in the range of 4.5–22 mm/yr is implied, even though this upper bound is not mentioned. An objective evaluation of these two previous studies shows that their authors sampled the loess cover (either OSL or ^{14}C dating) of the upper terrace surface, which likely postdates the abandonment of the terrace surface. The implication is that even though the upper terrace constrains the maximum age of offset accumulation, the loess cover age shifts the terrace age toward lower values. Therefore, several slip rates documented in previous studies have in fact larger uncertainties than asserted.

Strictly speaking, the true slip rate of the Haiyuan fault should lie between the ranges of the upper and lower bounds. It is thus helpful to explicitly distinguish the lower and upper bounds when reporting the rate. At the Daqing site in this study, the lower and the upper bounds of the slip rate, constrained by the offsets of the T3/T2 terrace riser top (>88 ± 9 m) and base (72 ± 3 m), and the respective upper (13.7 ± 1.5 ka) and lower (>9.3 ± 0.6 ka) terrace ages, are 6.4 ± 1 mm/yr and 7.7 ± 0.6 mm/yr. The different rates result from both the lower bound of the offset for the upper terrace (>88 ± 9 m) and the lower bound of the age for the lower terrace T2 (>9.3 ka; Table 5).

The terrace riser T2/T1 offset of 35 m provides a much larger uncertainty and looser constraint on the slip rate (3–27 mm/yr; Fig. 14). The contrast in slip rates bracketed by T3/T2 and T2/T1 at the same site highlights again that one should not favor the upper or the lower terrace reconstruction scenarios without additional information. If we use the upper terrace age as the offset age, the offset of the T3/T2 riser suggests a slip rate of 6.4 mm/yr (since 13.7 ka), whereas the offset of the T2/T1 riser suggests a slip rate of 3.5 mm/yr (since 9.3 ka), i.e., only half as much. This difference at the same site could be interpreted as a temporal change in slip rate, as has been suggested elsewhere for the Haiyuan or other faults (e.g., Weldon et al., 2004; Gold and Cowgill, 2011; Gold et al., 2017a; Liu et al., 2018). In reality, the rate estimates may be simply the lower and upper bounds, rather than true slip rates. The rate difference may be an indication of the variable initiation time of riser offset recorded after the abandonment of the upper terrace, and thus the uncertainty in slip-rate determination, rather than an indication of temporal change in slip behavior. A comparison between short- and long-term slip rates for several large strike-slip faults globally suggests that the slip rate does not change significantly through time (Cowgill et al., 2009; Meade et al., 2013; Tong et al., 2014).

Reducing Uncertainty in Slip-Rate Estimates from Terrace Riser Offsets

Terrace riser offsets may be measured in several ways to reduce uncertainties in slip rate. Although we can adopt both upper and lower terrace models to bracket a conservative slip rate range instead of seeking a true rate (Cowgill, 2007; Cowgill et al., 2009), large differences in the ages of the upper and lower terrace can produce a wide range of slip rates (e.g., Mériaux et al., 2012; Gold et al., 2017b). One way of reducing the uncertainty in slip rate is to lower the uncertainty in displacement bounds. In general, one measures offset riser paired tops (e.g., Hubert-Ferrari et al., 2002; Rizza et al., 2011; Gold et al., 2011) or middle parts (e.g., Mason et al., 2006; Carne et al., 2011) because of poor preservation of riser bases, which are locations of debris accumulation (Stewart et al., 2018), or one uses the full displacement range from the top, middle, and base of a riser (Gold et al., 2017b). In all cases, dividing such displacements by the ages of the lower terraces yields the high upper bounds of the slip rate.

The offset of the riser base is sometimes smaller than the offset of the riser top, like at our Daqing site and observed elsewhere (e.g., Gold et al., 2017b). In this case, rates determined by correlating the offset riser top and base with the ages of the upper and lower terraces, respectively, are more consistent, implying a vertical diachronicity. As illustrated in Figure 9G, the

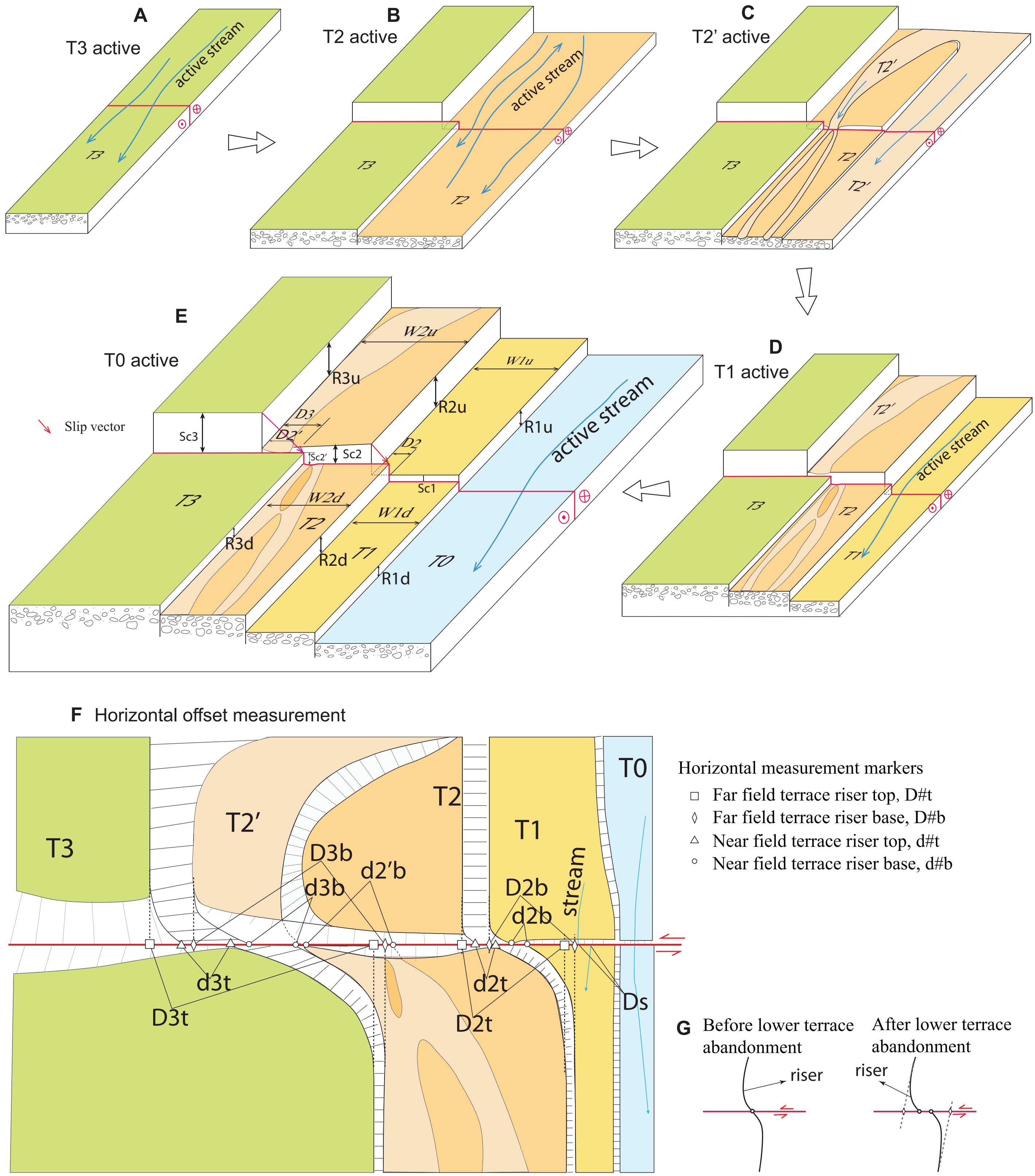

Figure 9. Offset terrace reconstructions. (A–E) Diagrams of different stages during river downcutting, lateral erosion, and displacement accumulation. Simplified risers are vertical. (F) Sketch of offset terraces at Daqing site. All measurement results are shown in Table 4. (G) Diagram showing how near-field (d3t, d3b, d2t, and d2b) and far-field displacements are related.

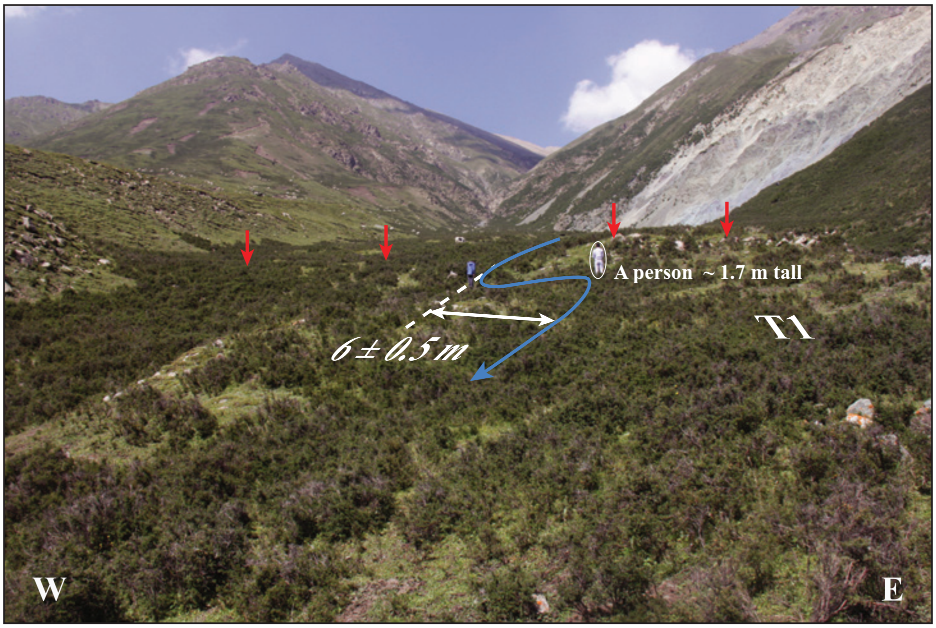

Figure 10. Field details of small stream offset on terrace T1. The location is shown in Figure 4. Red arrows indicate top of meter-high fault scarp across T1.

near-field offset was preserved after abandonment of the lower terrace when the stream had not totally refreshed the riser. The age of the lower terrace is close to or older than the time when the near-field displacement started to accumulate. The rate between the near-field offset and the age of the lower terrace abandonment may be close to the true slip rate, although it is strictly a lower bound (e.g., Mason et al., 2006; Zinke et al., 2017).

The advantage of multiple paired offset terraces to resolve such issues has long been demonstrated (e.g., Lensen, 1964; Sieh and Jahns, 1984; Weldon, 1986; Gaudemer et al., 1995; Van der Woerd et al., 1998, 2002). Consideration of a set of independently determined slip rates at a single site makes it possible to average the variability of river incision or lateral erosion with time. At the Daqing site, the set of four terrace levels allows such an approach. In our study, due to difficulties in determining the precise age of all the terrace levels, we nevertheless constrained their relative ages using one well-determined terrace age and their respective horizontal and vertical offsets.

Finally, to avoid the ambiguity in correlating terrace surface ages with their upper or lower risers, the offset of the terrace itself may be determined (e.g., Lensen, 1964; Peltzer et al., 1988, 2020). In general, this is possible when the terraces bear particular syndepositional geomorphic markers at their surface (channels, ridges) or if the terraces have specific inherited shapes (fan shapes, slopes) that enable unambiguous geometric reconstructions.

Stable Slip Vector with Time

The assumption of uniform slip rate over time implies that the average slip vector should be temporally stable (Cowgill, 2007). Thus, the ratio of vertical and horizontal offsets should also be constant for all terraces (Fig. 11; Table 5). The vertical offset of 15 ± 2 m and the minimum horizontal offset of 88 ± 9 m on T3 imply a maximum ratio of 0.170 ± 0.029. The ratios are 0.185 ± 0.068, 0.211 ± 0.05, and 0.2 ± 0.07 for T2, T2′, and T1, respectively. We consider an average ratio of 0.191 ± 0.018 to be consistent with the range of ratios for the four terraces (Fig. 11). This is larger than the ratio of 0.125 ± 0.025 estimated by Gaudemer et al. (1995) at this site, due to a determination of a larger total horizontal displacement of the upper terrace (T3, 145 m) based on the geometric reconstruction of the terrace from a small number of topographic profiles. Our terrace reconstruction, based on more exhaustive and high-resolution topographic data, suggests a smaller total horizontal offset for terrace T3 and a larger average ratio, consistent with the other terrace offsets (Table 5). When combining the ratio of 0.191 ± 0.018 and the vertical offset of 10 ± 1 m of T2, we can estimate the total horizontal displacement of T2 to about ~50 m, an offset larger than the T2/T1 riser offset (35 ± 2 m), but smaller than the T3/T2′ riser offset (72 ± 3 m). Although both the age and horizontal offset of T2 are not well determined, the fact that an ~50 m offset is not preserved further supports the lateral erosion of the T2/T1 riser after abandonment of T2 but prior to abandonment of T1.

Following the assumption of a temporally constant slip vector, our summary of measured offsets versus corresponding ages is compatible with a temporally uniform strike-slip rate of 4–7 mm/yr (light gray in Fig. 14) at this site (Table 5). Considering the tightly determined age of T3 and the far-field offset of the lower riser top (solid rectangle in Fig. 14), a rate of 5–8 mm/yr (dark gray in Fig. 14) may be preferred over the other less-well-determined data (dashed rectangles in Fig. 14).

Comparison with Geodetic Rates

It is tempting to favor the lower bound estimates for the Haiyuan fault slip rate, as they are closer to the geodetic rates from GPS data (4–5 mm/yr; Li et al., 2009) or from interferometric synthetic aperture radar (InSAR) data (4–8 mm/yr; Cavalié et al., 2008; Jolivet et al., 2013; Daout et al., 2016), as for the Altyn Tagh fault (Cowgill, 2007; Zhang et al., 2007; Gold et al., 2009, 2011). However, higher GPS or InSAR rates of 8.6 mm/yr have also been reported on the Haiyuan fault (Gan et al., 2007) and along the central section (Daout et al., 2016). Furthermore, discrepancies between geologic and geodetic slip rates have been found on other faults, such as the San Andreas fault (Chuang and Johnson, 2011; Johnson, 2013) and the Lazio-Abruzzo fault zone in central Italy (Papanikolaou et al., 2005).

These results remind us that the current GPS data are not targeted for optimal determination of fault slip rate, because instrumented sites

TABLE 5. SUMMARY OF SLIP RATES AT DAQING SITE

	Horizontal offset (m)	Vertical offset (m)	Ratio (vertical/horizontal)	Age (ka)	Horizontal slip rate (mm/yr)	Throw rate (mm/yr)
T1	6.5 ± 1.0	1.3 ± 0.2	0.2 ± 0.07	<1.3 ± 0.1 (bound)	>5.0 ± 0.9	>1.0 ± 0.2
T2′	28.5 ± 2.0	6.0 ± 1.5	0.211 ± 0.05	5.4 ± 1.0 (estimated)	5.3 ± 1.9	1.1 ± 0.5
T2	35 ± 2–72 ± 3	10 ± 1	0.185 ± 0.068	>9.3 ± 0.6 (bound)	5.8 ± 1.6	1.1 ± 0.1
T3	>88 ± 9	15 ± 2	<0.170 ± 0.029	13.7 ± 1.5	>6.4 ± 1.0	1.1 ± 0.2
Average			0.191 ± 0.018		5.6 ± 1.7 (4–7)	1.1 ± 0.1 (1.0–1.2)

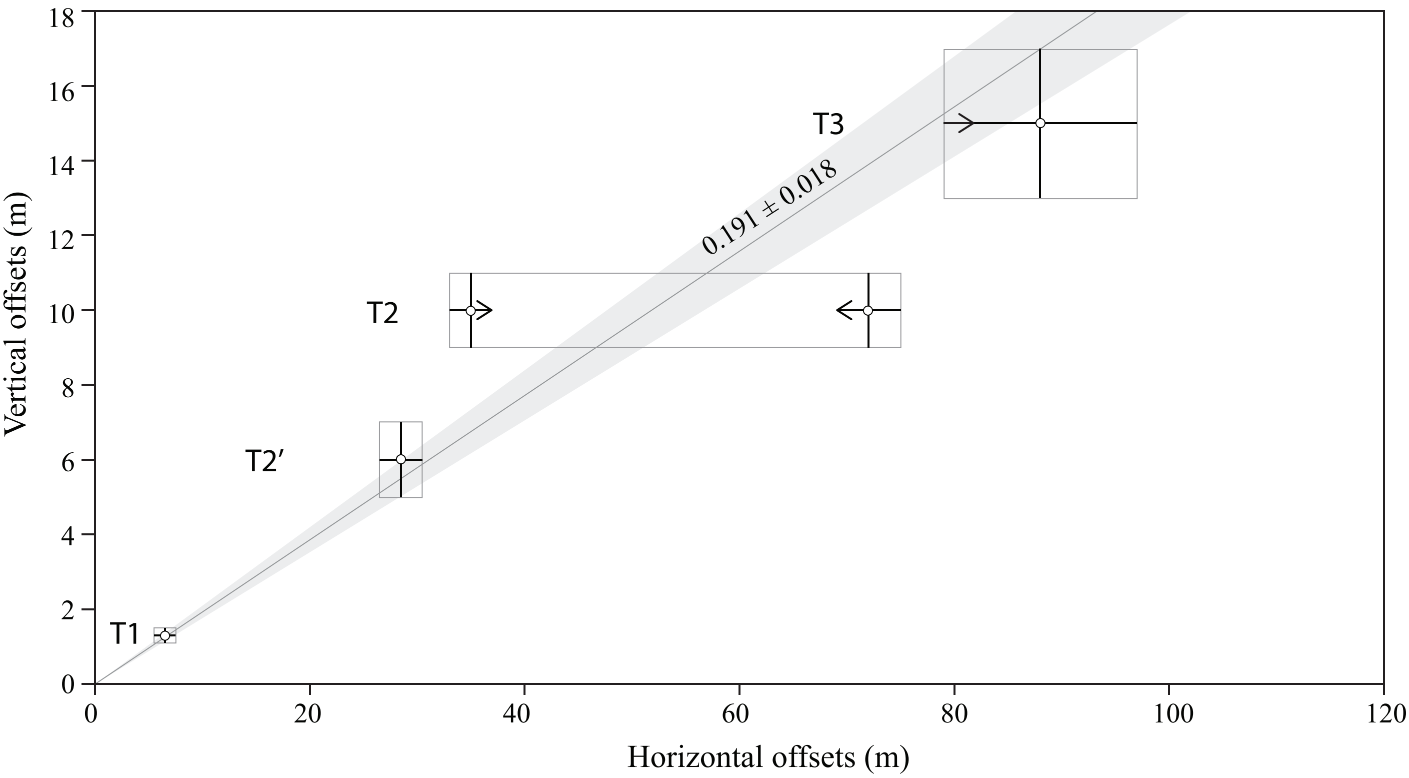

Figure 11. Vertical to horizontal offsets ratios for terraces T3, T2, T2′, and T1. Average ratio is 0.191 ± 0.018 (Table 5).

are still sparse, and thus the strain rate across single faults must be estimated by collapsing measurements within a wide (often 100-km-wide) swath. When doing so, the effects of fault geometry changes or fault interactions along strike are not taken into account. Overall, the best determined rate at the Daqing site (6.4 ± 1 mm/yr) falls within the range of geodetic rates (4–9 mm/yr) estimated for the Haiyuan fault system.

Implications for Earthquake Rupture History

The youngest faulted terrace, T1, with its inferred age of 1.3 ± 0.1 ka, implies that the age of the most recent rupture at this site is even younger. At the Daqing site, if terrace T1 and the streambed T0 experienced only one surface-rupturing event, as also speculated by Gaudemer et al. (1995), with the scarp across T0 being almost completely eroded, the offset of ~6.0 ± 0.5 m of the abandoned stream channel present on T1 and also the smallest lateral offset measured at the Daqing site may be considered as representative of the coseismic lateral slip of the last event. Combining the long-term slip rate of 5–8 mm/yr and this coseismic offset, the recurrence interval for such event would be 1100 ± 300 yr.

Previous paleoseismological work along fault segments adjacent to the Jin Qiang He segment concluded similar values for large earthquake recurrence. For the Lenglong Ling section west of our site, mean Holocene recurrence intervals of 1430 ± 140 yr (Jiang et al., 2017) and 1640 ± 570 yr (Guo et al., 2019) were derived from trench investigations. To the east of our site, paleoseismological investigations showed that the Laohu Shan section seemingly ruptures every ~1000 yr (Yuan et al., 1997; Liu-Zeng et al., 2007). However, only one event (after 3500 ± 200 yr B.P.) was identified in a trench along the Jin Qiang He section (Yuan et al., 1997). While more paleoseismological investigations are necessary to identify and precisely date the last large surface-rupturing events along the Jin Qiang He section of the Haiyuan fault, existing data and our inference from terrace T1 at the Daqing site concur with the occurrence of a large event in the past 1000 yr and possible return times of 1000–2000 yr for large earthquakes.

The Jin Qiang He section is ~55 km long. If this section ruptures entirely, the magnitude could reach up to Mw 7.1, or if a maximum coseismic displacement of 6 m is considered, the magnitude could reach up to Mw 7.4, according to empirical relationships among surface rupture length, maximum displacement, and magnitude (Wells and Coppersmith, 1994). If the rupture breaches the 6-km-wide Tianzhu stepover and propagates to the western part of the Maomao Shan section, the rupture length could reach 120 km and s maximum magnitude Mw 7.5 (Wells and Coppersmith, 1994). Although

Figure 12. Exposure age constraint for terrace T3 at Daqing site. (A–C) Proposed stepwise evolution of deposit for terrace T3 ^{10}Be depth profile modeling. (D–F) Terrace T3 ^{10}Be depth profile modeling, where t_{1-1}, t_{2-1}, and t_{3-1} are corresponding terrace abandonment ages for models 1, 2, and 3; R-squared is statistical assessment of ^{10}Be data with respect to best fit, without outliers (black circles). Integrated density (thick black line) and average inheritance are indicated. (A, D) Model 1: assumes all layers were deposited in one step (I). (B, E) Model 2: exposure in three steps: (I) terrace conglomerate only (t_{2-1} to t_{2-2}), (II) with 30-cm-thick sandy-loess (t_{2-2} to t_{2-3}), and (III) with 80-cm-thick soil (t_{2-3} to 0). Assumes all layers were deposited instantaneously. (C, F) Model 3: same as model 2, but assumes layers were deposited progressively, as constrained by optically stimulated luminescence (OSL) and ^{14}C dates.

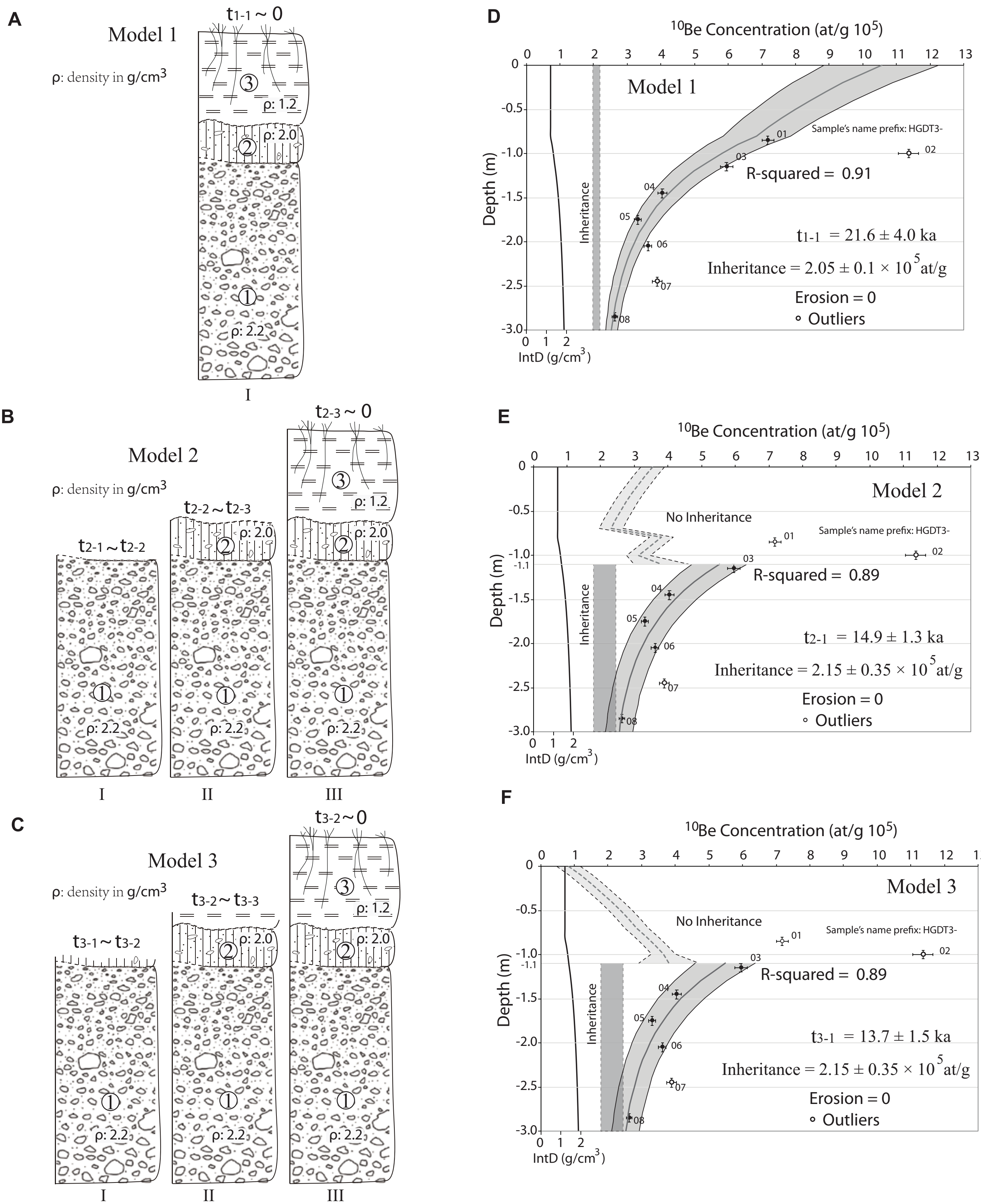
A
Model 1
ρ: density in g/cm3
t1-1 ~ 0
ρ: 1.2
ρ: 2.0
ρ: 2.2
I
B
Model 2
ρ: density in g/cm3
t2-1 ~ t2-2
t2-2 ~ t2-3
t2-3 ~ 0
I
II
III
C
Model 3
ρ: density in g/cm3
t3-1 ~ t3-2
t3-2 ~ t3-3
t3-2 ~ 0
D
10Be Concentration (at/g 10^5)
Depth (m)
IntD (g/cm3)
Model 1
Inheritance
Sample's name prefix: HGDT3-
R-squared = 0.91
t1-1 = 21.6 ± 4.0 ka
Inheritance = 2.05 ± 0.1 × 10^5 at/g
Erosion = 0
Outliers
E
Model 2
No Inheritance
R-squared = 0.89
t2-1 = 14.9 ± 1.3 ka
Inheritance = 2.15 ± 0.35 × 10^5 at/g
Erosion = 0
Outliers
F
Model 3
No Inheritance
R-squared = 0.89
t3-1 = 13.7 ± 1.5 ka
Inheritance = 2.15 ± 0.35 × 10^5 at/g
Erosion = 0
Outliers

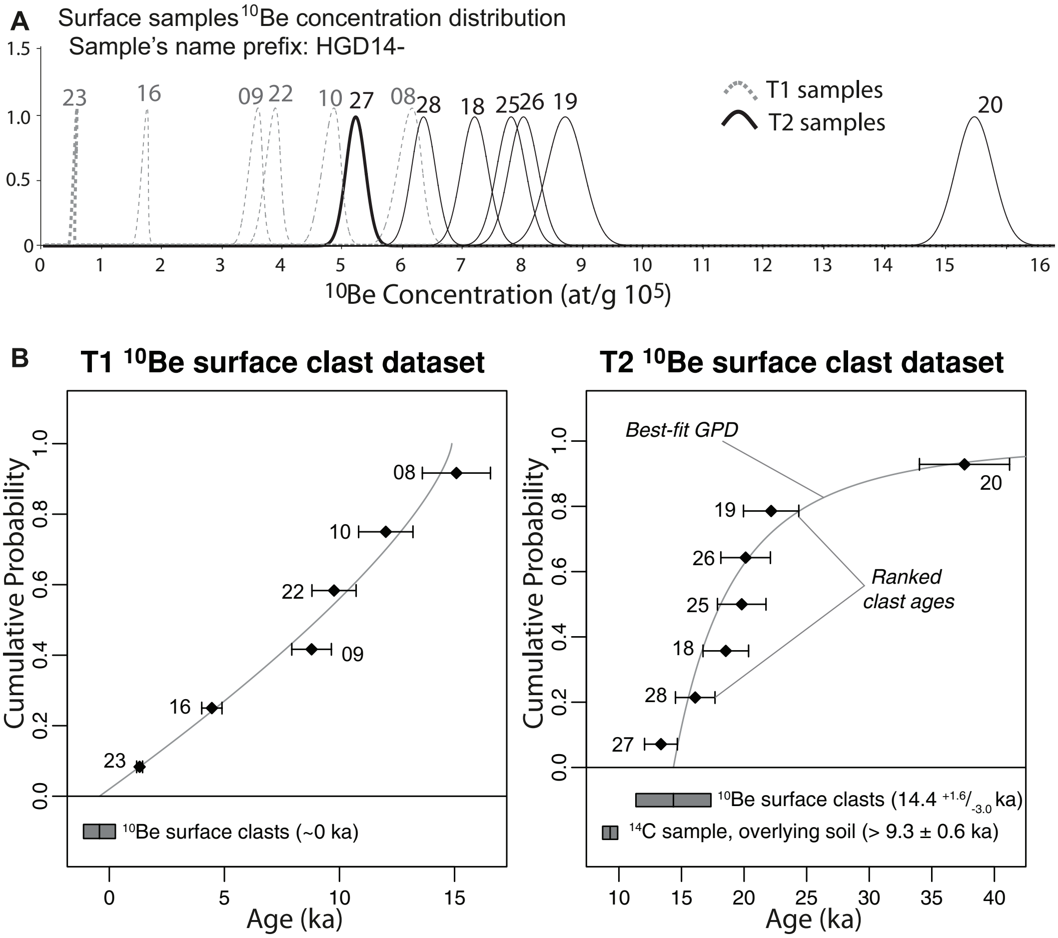

Figure 13. Exposure age constraints for terraces T1 and T2 at Daqing site. (A) ^{10}Be concentrations of surface samples from terraces T1 (*n* = 6) and T2 (*n* = 7) represented as Gaussian distributions. Scatter of sample ages is attributed to inheritance (see text). Bold lines are samples with lowest ^{10}Be concentration in each population (HGD14-23 and HGD14-27). (B) Model of boulder ages using the inheritance model of Prush and Oskin (2020). GPD—generalized Pareto distribution of inheritance. Model surface age is the lower bound of the GPD, with uncertainty determined by Monte Carlo Markov chain simulation of distribution parameter fit.

breaching such stepovers may be difficult (e.g., Wesnousky, 2006; Yıkılmaz et al., 2015), cascading stepping ruptures are not unusual (e.g., Tocheport et al., 2006; Xu et al., 2008; Hamling et al., 2017; Fletcher et al., 2014). Thus, the Jin Qiang He and adjacent sections could rupture simultaneously in a future great earthquake. Precise seismic risk assessment demands further detailed paleoseismological investigations be carried out to define the rupture history along the central Haiyuan fault.

CONCLUSION

High-resolution topography data derived from terrestrial LiDAR and structure-from-motion photogrammetry enabled us to investigate in detail the offset features at the Daqing site along the Jin Qiang He section of the Haiyuan fault. Terraces T1, T2′, T2, and T3 were carefully mapped from field observations, orthophotos, and topographic data to produce a detailed geomorphic map of the site. Far- and near-field projections, top and base, for the various riser offsets were measured, as well as the vertical offset of the terraces. Horizontal offsets ranged from 6 to 97 m, and vertical offsets ranged from 1 to 17 m. The smallest horizontal offset of 6.0 ± 0.5 m may be associated with the most recent coseismic slip. Terrestrial cosmogenic nuclide dating combined with ^{14}C and OSL dating were used to constrain the age of the highest terrace (T3) at 13.7 ± 1.5 ka. Together with the offset of terrace riser T3/T2 of 88 ± 9 m, this yielded a left-lateral slip rate of 6.4 ± 1.0 mm/yr. The offset of 72 ± 3 m of the T3/T2 riser base, using the minimum age of the lower terrace (9.3 ± 0.6 ka), yielded a maximum rate of 7.7 ± 0.6 mm/yr. These bounds bracket a geologic slip rate of 5–8 mm/yr for the Haiyuan fault, which is similar to the bounds estimated from geodetic data. Overall, compared to preexisting geological rates, our rate falls in between the lower and higher estimates. At the Daqing site, the ratio of vertical and horizontal offsets of all terraces (~1:5.2) is consistent with a uniform slip vector over time. The Daqing site provides an example where right-bank terrace risers cut by a left-lateral fault, i.e., displaced toward the active channel, are subject to incomplete refreshment and partial preservation.

ACKNOWLEDGMENTS

This work was jointly funded by the National Natural Science Foundation of China (41802228, U1839203), the Innovation Team Special Project of Gansu Earthquake Agency (Research Group of Active Tectonics and Geohazard in Western China), and the Science for Earthquake Resilience of China Earthquake Administration (XH19044), and Y. Shao was partly supported by a grant from the K.C. Wong Foundation and the Centre National de la Recherche Scientifique (CNRS). Klinger was partly supported by the China-France Projet International de Cooperation Scientifique (PICS) program from CNRS. *GF-1* satellite imagery was offered by Wang Lin from the Institute of Earthquake Science, China Earthquake Administration. We thank Alex Morelan and Veronica Prush at the University of California–Davis for their advice on sample age analysis. Veronica Prush also helped to model the surface ages. We are grateful to the ASTER Team (G. Aumaître, D. Bourlès, and K. Keddadouche) at ASTER–Centre Européen de Recherche et d'Enseignement des Géosciences de l'Environnement (CEREGE) for accelerator mass spectrometry measurements. This work was financially supported by l'Institut National des Sciences de l'Univers (INSU), CNRS, France, and the University of Strasbourg (to J. Van der Woerd) for the Al and Be concentration analyses at the Laboratoire d'Hydrologie et de Geochimie de Strasbourg and Institut de Physique du Globe de Strasbourg, and for

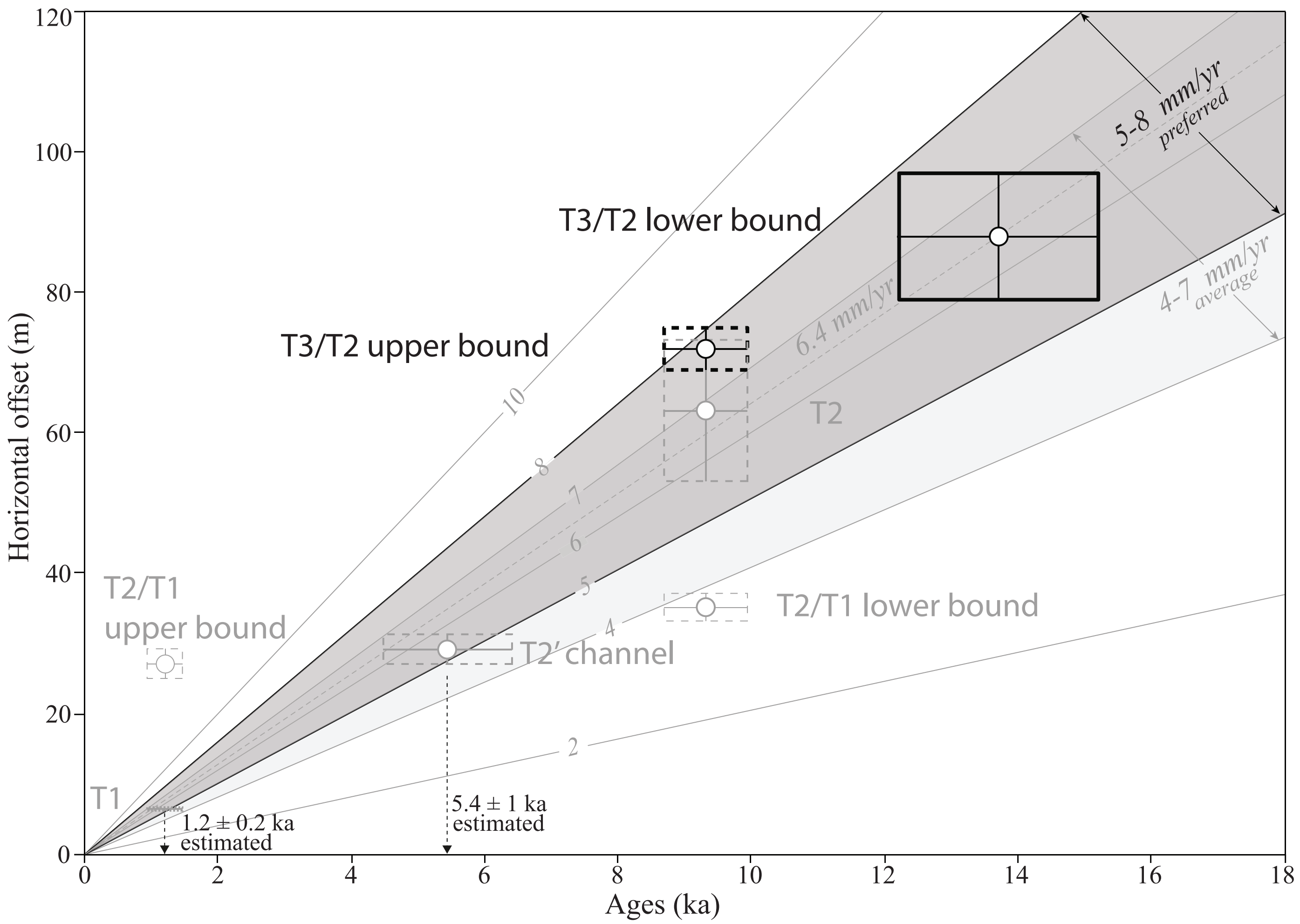

Figure 14. Summary of terrace offsets at Daqing He site as a function of age. Solid rectangle is best determined rate from terrace T3. Dashed rectangles are less well determined. Light-gray shaded area is average rate; dark gray is preferred slip rate range.

the $^{10}Be/^{9}Be$ ratio measurements at the ASTER AMS facility (CEREGE, Aix-en-Provence, France), supported by INSU-CNRS and l'Institut de Recherche pour le Développement (IRD).

REFERENCES CITED

Aitken, M.J., 1998, Introduction to Optical Dating: The Dating of Quaternary Sediments by the Use of Photon-Stimulated Luminescence: Oxford, UK, Clarendon Press, 267 p.

Arrowsmith, J.R., and Zielke, O., 2009, Tectonic geomorphology of the San Andreas fault zone from high resolution topography: An example from the Cholame section: Geomorphology, v. 113, p. 70–81, https://doi.org/10.1016/j.geomorph.2009.01.002.

Balco, G., Stone, J.O., Lifton, N.A., and Dunai, T.J., 2008, A complete and easily accessible means of calculating surface exposure ages or erosion rates from ^{10}Be and ^{26}Al measurements: Quaternary Geochronology, v. 3, p. 174–195, https://doi.org/10.1016/j.quageo.2007.12.001.

Bemis, S.P., Micklethwaite, S., Turner, D., James, M.R., Akciz, S., Thiele, S.T., and Bangash, H.A., 2014, Ground-based and UAV-based photogrammetry: A multi-scale, high-resolution mapping tool for structural geology and paleoseismology: Journal of Structural Geology, v. 69, p. 163–178, https://doi.org/10.1016/j.jsg.2014.10.007.

Benedetti, L.C., and Van der Woerd, J., 2014, Cosmogenic nuclide dating of earthquakes, faults, and toppled blocks: Elements, v. 10, no. 5, p. 357–361, https://doi.org/10.2113/gselements.10.5.357.

Berryman, K., 1990, Late Quaternary movement on the Wellington fault in the Upper Hutt area, New Zealand: New Zealand Journal of Geology and Geophysics, v. 33, no. 2, p. 257–270, https://doi.org/10.1080/00288306.1990.10425683.

Borchers, B., Marrero, S., Balco, G., Caffee, M., Goehring, B., Lifton, N., Nishiizumi, K., Phillips, F., Schaefer, J., and Stone, J., 2016, Geological calibration of spallation production rates in the CRONUS-Earth project: Quaternary Geochronology, v. 31, p. 188–198, https://doi.org/10.1016/j.quageo.2015.01.009.

Braucher, R., Guillou, V., Bourlès, D.L., Arnold, M., Aumaître, G., Keddadouche, K., and Nottoli, E., 2015, Preparation of ASTER in-house $^{10}Be/^{9}Be$ standard solutions: Nuclear Instruments & Methods in Physics Research, Section B, Beam Interactions with Materials and Atoms, v. 361, p. 335–340, https://doi.org/10.1016/j.nimb.2015.06.012.

Burchfiel, B.C., Quidong, D., Molnar, P., Royden, L., Yipeng, W., Peizhen, Z., and Weiqi, Z., 1989, Intracrustal detachment within zones of continental deformation: Geology, v. 17, no. 8, p. 748–752, https://doi.org/10.1130/0091-7613(1989)017<0448:IDWZOC>2.3.CO;2.

Carne, R.C., Little, T.A., and Rieser, U., 2011, Using displaced river terraces to determine late Quaternary slip rate for the central Wairarapa fault at Waiohine River, New Zealand: New Zealand Journal of Geology and Geophysics, v. 54, no. 2, p. 217–236, https://doi.org/10.1080/00288306.2010.532224.

Carretier, S., Regard, V., Vassallo, R., Martinod, J., Christophoul, F., Gayer, E., Audin, L., and Lagane, C., 2015, A note on ^{10}Be-derived mean erosion rates in catchments with heterogeneous lithology: Examples from the western Central Andes: Earth Surface Processes and Landforms, v. 40, no. 13, p. 1719–1729, https://doi.org/10.1002/esp.3748.

Cavalié, O., Lasserre, C., Doin, M.-P., Peltzer, G., Sun, J., Xu, X., and Shen, Z.-K., 2008, Measurement of interseismic strain across the Haiyuan fault (Gansu, China), by InSAR: Earth and Planetary Science Letters, v. 275, p. 246–257, https://doi.org/10.1016/j.epsl.2008.07.057.

Chen, T., Zhang, P.Z., Liu, J., Li, C.Y., Ren, Z.K., and Hudnut, K.W., 2014, Quantitative study of tectonic geomorphology along Haiyuan fault based on airborne LiDAR: Chinese Science Bulletin, v. 59, no. 20, p. 2396–2409, https://doi.org/10.1007/s11434-014-0199-4.

Chen, T., Akciz, S.O., Hudnut, K.W., Zhang, D.Z., and Stock, J.M., 2015, Fault-slip distribution of the 1999 Mw 7.1 Hector Mine earthquake, California, estimated from postearthquake airborne LiDAR data: Bulletin of the Seismological Society of America, v. 105, no. 2A, p. 776–790, https://doi.org/10.1785/0120130108.

Chen, T., Liu-Zeng, J., Shao, Y., Zhang, P., Oskin, M.E., Lei, Q., and Li, Z., 2018, Geomorphic offsets along the creeping Laohu Shan section of the Haiyuan fault, northern Tibetan Plateau: Geosphere, v. 14, no. 3, p. 1165–1186, https://doi.org/10.1130/GES01561.1.

Chevalier, M.L., Leloup, P.H., Replumaz, A., Pan, J., Liu, D., Li, H., Gourbet, L., and Métois, M., 2016, Tectonic-geomorphology of the Litang fault system, SE Tibetan Plateau, and implication for regional seismic hazard: Tectonophysics, v. 682, p. 278–292, https://doi.org/10.1016/j.tecto.2016.05.039.

Chmeleff, J., von Blanckenburg, F., Kossert, K., and Jakob, D., 2010, Determination of the ^{10}Be half-life by multicollector ICP-MS and liquid scintillation counting: Nuclear Instruments & Methods in Physics Research, Section B, Beam Interactions with Materials and Atoms, v. 268, p. 192–199, https://doi.org/10.1016/j.nimb.2009.09.012.

Chuang, R.Y., and Johnson, K.M., 2011, Reconciling geologic and geodetic model fault slip-rate discrepancies in Southern California: Consideration of nonsteady mantle flow and lower crustal fault creep: Geology, v. 39, no. 7, p. 627–630, https://doi.org/10.1130/G32120.1.

Clark, K., Nissen, E., Howarth, J., Hamling, I., Mountjoy, J., Ries, W., Jones, K., Goldstein, S., Cochran, U., Villamor, P., Hreinsdóttir, S., Litchfield, N., Mueller, C., Berryman, K., and Strong, D., 2017, Highly variable coastal deformation in the 2016 Mw 7.8 Kaikōura earthquake reflects rupture complexity along a transpressional plate boundary: Earth and Planetary Science Letters, v. 474, p. 334–344, https://doi.org/10.1016/j.epsl.2017.06.048.

Cowgill, E., 2007, Impact of riser reconstructions on estimation of secular variation in rates of strike-slip faulting: Revisiting the Cherchen River site along the Altyn Tagh fault, NW China: Earth and Planetary Science Letters, v. 254, p. 239–255, https://doi.org/10.1016/j.epsl.2006.09.015.

Cowgill, E., Gold, R.D., Xuanhua, C., Xiao-Feng, W., Arrowsmith, J.R., and Southon, J., 2009, Low Quaternary slip rate reconciles geodetic and geologic rates along the Altyn Tagh fault, northwestern Tibet: Geology, v. 37, no. 7, p. 647–650, https://doi.org/10.1130/G25623A.1.

Daëron, M., Benedetti, L., Tapponnier, P., Sursock, A., and Finkel, R.C., 2004, Constraints on the post ~25-ka slip rate of the Yammoûneh fault (Lebanon) using in situ cosmogenic ^{36}Cl dating of offset limestone-clast fans: Earth and Planetary Science Letters, v. 227, p. 105–119, https://doi.org/10.1016/j.epsl.2004.07.014.

Daout, S., Jolivet, R., Lasserre, C., Doin, M.P., Barbot, S., Tapponnier, P., Peltzer, G., Socquet, A. and Sun, J., 2016, Along-strike variations of the partitioning of convergence across the Haiyuan fault system detected by InSAR: Geophysical Journal International, v. 205, p. 536–547, https://doi.org/10.1093/gji/ggw028.

Deng, Q., Sung, F., Zhu, S., Li, M., Wang, T., Zhang, W., Burchfiel, B.C., Molnar, P., and Zhang, P., 1984, Active faulting and tectonics of the Ningxia-Hui autonomous region, China: Journal of Geophysical Research, v. 89, p. 4427–4445, https://doi.org/10.1029/JB089iB06p04427.

Division of Earthquake Monitoring and Prediction, State Seismologic Bureau, 1995, Catalog of Chinese Historical Strong Earthquakes (2300 B.C.–1911 A.D.), China: Beijing, Seismological Press, 514 p.

Duvall, A.R., Clark, M.K., Kirby, E., Farley, K.A., Craddock, W.H., Li, C., and Yuan, D.Y., 2013, Low-temperature thermochronometry along the Kunlun and Haiyuan faults, NE Tibetan Plateau: Evidence for kinematic change during late-stage orogenesis: Tectonics, v. 32, no. 5, p. 1190–1211, https://doi.org/10.1002/tect.20072.

England, P., and Molnar, P., 1997, The field of crustal velocity in Asia calculated from Quaternary rates of slip on faults: Geophysical Journal International, v. 130, no. 3, p. 551–582, https://doi.org/10.1111/j.1365-246X.1997.tb01853.x.

Fletcher, J.M., Teran, O.J., Rockwell, T.K., Oskin, M.E., Hudnut, K.W., Mueller, K.J., Spelz, R.M., Akciz, S.O., Masana, E., Faneros, Fielding, E.J., Leprince, S., Morelan, A.E., Stock, J., Lynch, D.K., Elliott, A.J., Gold, P., Liu-Zeng, J., González-Ortega, A., Hinojosa-Corona, A., an González-García, J., 2014, Assembly of a large earthquake from a complex fault system: Surface rupture kinematics of the 4 April 2010 El Mayor–Cucapah (Mexico) Mw7.2 earthquake: Geosphere, v. 10, p. 797–827, https://doi.org/10.1130/GES00933.1.

Galbraith, R.F., and Roberts, R.G., 2012, Statistical aspects of equivalent dose and error calculation and display in OSL dating: An overview and some recommendations: Quaternary Geochronology, v. 11, p. 1–27, https://doi.org/10.1016/j.quageo.2012.04.020.

Gan, W., Zhang, P.Z., Shen, Z.-K., Niu, Z., Wang, M., Wan, Y., Zhou, D., and Cheng, J., 2007, Present-day crustal motion within the Tibetan Plateau inferred from GPS measurements: Journal of Geophysical Research, v. 112, no. B8, B08416, https://doi.org/10.1029/2005JB004120.

Gaudemer, Y., Tapponnier, P., and Turcotte, D.L., 1989, River offsets across active strike-slip faults: Annales Tectonicae, v. 3, no. 3, p. 55–76.

Gaudemer, Y., Tapponnier, P., Meyer, B., Peltzer, G., Guo Shunmin, Chen Zhitai, Dai Huagung, and Cifuentes, I., 1995, Partitioning of crustal slip between linked, active faults in the eastern Qilianshan, and evidence for a major seismic gap, the 'Tianzhu gap,' on the western Haiyuan fault, Gansu (China): Geophysical Journal International, v. 120, p. 599–645, https://doi.org/10.1111/j.1365-246X.1995.tb01842.x.

Gold, R.D., and Cowgill, E., 2011, Deriving fault-slip histories to test for secular variation in slip, with examples from the Kunlun and Awatere faults: Earth and Planetary Science Letters, v. 301, no. 1–2, p. 52–64, https://doi.org/10.1016/j.epsl.2010.10.011.

Gold, R.D., Cowgill, E., Arrowsmith, J.R., Gosse, J., Chen, X., and Wang, X.-F., 2009, Riser diachroneity, lateral erosion, and uncertainty in rates of strike-slip faulting: A case study from Tuzidun along the Altyn Tagh fault, NW China: Journal of Geophysical Research–Solid Earth, v. 114, no. B4, B04401, https://doi.org/10.1029/2008JB005913.

Gold, R.D., Cowgill, E., Arrowsmith, J.R., Chen, X., Sharp, W.D., Cooper, K.M., and Wang, X.F., 2011, Faulted terrace risers place new constraints on the late Quaternary slip rate for the central Altyn Tagh fault, northwest Tibet: Geological Society of America Bulletin, v. 123, no. 5–6, p. 958–978, https://doi.org/10.1130/B30207.1.

Gold, R.D., Cowgill, E., Arrowsmith, J.R., and Friedrich, A.M., 2017a, Pulsed strain release on the Altyn Tagh fault, northwest China: Earth and Planetary Science Letters, v. 459, p. 291–300, https://doi.org/10.1016/j.epsl.2016.11.024.

Gold, R.D., Briggs, R.W., Crone, A.J., and DuRoss, C.B., 2017b, Refining fault slip rates using multiple displaced terrace risers—An example from the Honey Lake fault, NE California, USA: Earth and Planetary Science Letters, v. 477, p. 134–146, https://doi.org/10.1016/j.epsl.2017.08.021.

Guo, P., Han, Z., Mao, Z., Xie, Z., Dong, S., Gao, F., and Gai, H., 2019, Paleoearthquakes and rupture behavior of the Lenglongling fault: Implications for seismic hazards of the northeastern margin of the Tibetan Plateau: Journal of Geophysical Research–Solid Earth, v. 124, no. 2, p. 1520–1543, https://doi.org/10.1029/2018JB016586.

Hamling, I.J., Hreinsdóttir, S., Clark, K., et al., 2017, Complex multifault rupture during the 2016 Mw7.8 Kaikoura earthquake, New Zealand: Science, v. 356, no. 6334, p. eaam7194, https://doi.org/10.1126/science.aam7194.

Harkins, N., and Kirby, E., 2008, Fluvial terrace riser degradation and determination of slip rates on strike-slip faults: An example from the Kunlun fault, China: Geophysical Research Letters, v. 35, L05406, https://doi.org/10.1029/2007GL033073.

He, W.G., Liu, B.C., Yuan, D.Y., and Yang, M., 2000, Study on the slip rate of Lenglongling active fault zone: Northwestern Seismological Journal, v. 22, no. 1, p. 90–97 [in Chinese].

He, W.G., Yuan, D.Y., Ge, W.P., and Luo, H., 2010, Determination of the slip rate of the Lenglongling fault in the middle and eastern segments of the Qilian Mountain active fault zone: Earthquake, v. 30, no. 1, p. 131–137 [in Chinese].

Heimsath, A.M., and McGlynn, R., 2008, Quantifying periglacial erosion in the Nepal High Himalaya: Geomorphology, v. 97, no. 1–2, p. 5–23, https://doi.org/10.1016/j.geomorph.2007.02.046.

Hetzel, R., 2013, Active faulting, mountain growth, and erosion at the margins of the Tibetan Plateau constrained by in situ–produced cosmogenic nuclides: Tectonophysics, v. 582, p. 1–24, https://doi.org/10.1016/j.tecto.2012.10.027.

Hetzel, R., Tao, M., Stokes, S., Niedermann, S., Ivy-Ochs, S., Gao, B., Strecker, M.R., and Kubik, P.W., 2004, Late Pleistocene/Holocene slip rate of the Zhangye thrust (Qilian Shan, China) and implications for the active growth of the northeastern Tibetan Plateau: Tectonics, v. 23, no. 6, TC6006, https://doi.org/10.1029/2004TC001653.

Hetzel, R., Hampel, A., Gebbeken, P., Xu, Q., and Gold, R.D., 2019, A constant slip rate for the western Qilian Shan frontal thrust during the last 200 ka consistent with GPS-derived and geological shortening rates: Earth and Planetary Science Letters, v. 509, p. 100–113, https://doi.org/10.1016/j.epsl.2018.12.032.

Heyman, J., Stroeven, A.P., Harbor, J.M., and Caffee, M.W., 2011, Too young or too old: Evaluating cosmogenic exposure dating based on an analysis of compiled boulder exposure ages: Earth and Planetary Science Letters, v. 302, p. 71–80, https://doi.org/10.1016/j.epsl.2010.11.040.

Hubert-Ferrari, A., Armijo, R., King, G., Meyer, B., and Barka, A., 2002, Morphology, displacement, and slip rates along the North Anatolian fault, Turkey: Journal of Geophysical Research–Solid Earth, v. 107, no. B10, 2235, https://doi.org/10.1029/2001JB000393.

Hudnut, K.W., Borsa, A., Glennie, C., and Minster, J.B., 2002, High-resolution topography along surface rupture of the 16 October 1999 Hector Mine, California, earthquake (Mw 7.1) from airborne laser swath mapping: Bulletin of the Seismological Society of America, v. 92, no. 4, p. 1570–1576.

James, M.R., and Robson, S., 2012, Straightforward reconstruction of 3D surfaces and topography with a camera: Accuracy and geoscience application: Journal of Geophysical Research–Earth Surface, v. 117, F03017, https://doi.org/10.1029/2011JF002289.

Jiang, W., Han, Z., Guo, P., Zhang, J., Jiao, Q., Kang, S., and Tian, Y., 2017, Slip rate and recurrence intervals of the east Lenglongling fault constrained by morphotectonics: Tectonic implications for the northeastern Tibetan Plateau: Lithosphere, v. 9, no. 3, p. 417–430, https://doi.org/10.1130/L597.1.

Johnson, K.M., 2013, Slip rates and off-fault deformation in Southern California inferred from GPS data and models: Journal of Geophysical Research–Solid Earth, v. 118, no. 10, p. 5643–5664, https://doi.org/10.1002/jgrb.50365.

Jolivet, R., Lasserre, C., Doin, M.P., Peltzer, G., Avouac, J.P., Sun, J., and Dailu, R., 2013, Spatio-temporal evolution of aseismic slip along the Haiyuan fault, China: Implications for fault frictional properties: Earth and Planetary Science Letters, v. 377, p. 23–33, https://doi.org/10.1016/j.epsl.2013.07.020.

Kirby, E., Harkins, N., Wang, E., Shi, X., Fan, C., and Burbank, D., 2007, Slip rate gradients along the eastern Kunlun fault: Tectonics, v. 26, TC2010, https://doi.org/10.1029/2006TC002033.

Klinger, Y., Etchebes, M., Tapponnier, P., and Narteau, C., 2011, Characteristic slip for five great earthquakes along the Fuyun fault in China: Nature Geoscience, v. 4, no. 6, p. 389–392, https://doi.org/10.1038/ngeo1158.

Knuepfer, P.L., 1992, Temporal variations in latest Quaternary slip across the Australian-Pacific plate boundary, northeastern South Island, New Zealand: Tectonics, v. 11, no. 3, p. 449–464, https://doi.org/10.1029/91TC02890.

Korschinek, G., Bergmaier, A., Faestermann, T., Gerstmann, U.C., Knie, K., Rugel, G., Wallner, A., Dillmann, I., Dollinger, G., von Gostomski, C.L., Kossert, K., Maiti, M., Poutivtsev, M., and Remmert, A., 2010, A new value for the half-life of ^{10}Be by heavy-ion elastic recoil detection and liquid scintillation counting: Nuclear Instruments & Methods in Physics Research, Section B, Beam Interactions with Materials and Atoms, v. 268, p. 187–191, https://doi.org/10.1016/j.nimb.2009.09.020.

Küster, Y., Hetzel, R., Krbetschek, M., and Tao, M., 2006, Holocene loess sedimentation along the Qilian Shan (China): Significance for understanding the processes and timing of loess deposition: Quaternary

Science Reviews, v. 25, no. 1, p. 114–125, https://doi.org/10.1016/j.quascirev.2005.03.003.

Lal, D., 1991, Cosmic ray labeling of erosion surfaces: In situ nuclide production rates and erosion models: Earth and Planetary Science Letters, v. 104, p. 424–439, https://doi.org/10.1016/0012-821X(91)90220-C.

Langridge, R.M., Rowland, J., Villamor, P., Mountjoy, J., Townsend, D.B., Nissen, E., Madugo, C., Ries, W.F., Gasston, C., Canva, A., Alexandra, E., Hatem, A.E., and Hamling, I., 2018, Coseismic rupture and preliminary slip estimates for the Papatea fault and its role in the 2016 Mw 7.8 Kaikōura, New Zealand, earthquake: Bulletin of the Seismological Society of America, v. 108, no. 3B, p. 1596–1622, https://doi.org/10.1785/0120170336.

Lasserre, C., Morel, P.H., Gaudemer, Y., Tapponnier, P., Ryerson, F.J., King, G.C.P., Metivier, F., Kasser, M., Kashgariana, M., Liu, B., Lu, T., and Yuan, D., 1999, Postglacial left slip rate and past occurrence of M≥8 earthquakes on the western Haiyuan fault, Gansu, China: Journal of Geophysical Research, v. 104, no. B8, p. 17633–17651, https://doi.org/10.1029/1998JB900082.

Lasserre, C., Gaudemer, Y., Tapponnier, P., Mériaux, A.-S., Van der Woerd, J., Yuan, D., Ryerson, F.J., Finkel, R.C., and Caffee, M.W., 2002, Fast late Pleistocene slip rate on the Lenglongling section of the Haiyuan fault, Qinghai, China: Journal of Geophysical Research, v. 107, no. B11, 2276, https://doi.org/10.1029/2000JB000060.

Le Béon, M., Klinger, Y., Mériaux, A.S., Al-Qaryouti, M., Finkel, R.C., Mayyas, O., and Tapponnier, P., 2012, Quaternary morphotectonic mapping of the Wadi Araba and implications for the tectonic activity of the southern Dead Sea fault: Tectonics, v. 31, no. 5, TC5003, https://doi.org/10.1029/2012TC003112.

Le Dortz, K., Meyer, B., Sébrier, M., Braucher, R., Nazari, H., Benedetti, L., Fattahi, M., Bourlès, D., Foroutan, M., Siame, L., and Rashidi, A., 2011, Dating inset terraces and offset fans along the Dehshir fault (Iran) combining cosmogenic and OSL methods: Geophysical Journal International, v. 185, no. 3, p. 1147–1174, https://doi.org/10.1111/j.1365-246X.2011.05010.x.

Le Dortz, K., Meyer, B., Sébrier, M., Braucher, R., Bourlès, D., Benedetti, L., Nazari, H., and Foroutan, M., 2012, Interpreting scattered in-situ produced cosmogenic nuclide depth-profile data: Quaternary Geochronology, v. 11, p. 98–115, https://doi.org/10.1016/j.quageo.2012.02.020.

Lensen, G.J., 1964, The general case of progressive fault displacement of flights of degradational terraces: New Zealand Journal of Geology and Geophysics, v. 7, no. 4, p. 864–870, https://doi.org/10.1080/00288306.1964.10428134.

Lensen, G.J., 1968, Analysis of progressive fault displacement during downcutting at the Branch River terraces, South Island, New Zealand: Geological Society of America Bulletin, v. 79, no. 5, p. 545–556, https://doi.org/10.1130/0016-7606(1968)79[545:AOPFDD]2.0.CO;2.

Li, C., Zhang, P.Z., Yin, J., and Min, W., 2009, Late Quaternary left-lateral slip rate of the Haiyuan fault, northeastern margin of the Tibetan Plateau: Tectonics, v. 28, no. 5, TC5010, https://doi.org/10.1029/2008TC002302.

Liang, S.M., Zheng, W.J., and Chen, G., 2018, Offset distribution and slip rate of the Jinqianghe fault of the Qilian–Haiyuan fault zone, *in* Annual Meeting of Chinese Geoscience Union, Abstracts [in Chinese].

Liu, J.R., Ren, Z.K., Zhang, H.P., Li, C.Y., Zhang, Z.Q., Zheng, W.J., Li, X.M., and Liu, C.C., 2018, Late Quaternary slip rate of the Laohushan fault within the Haiyuan fault zone and its tectonic implications: Chinese Journal of Geophysics, v. 61, no. 4, p. 1281–1297 [in Chinese], https://doi.org/10.6038/cjg2018L0364.

Liu-Zeng, J., Klinger, Y., Xu, X., Lasserre, C., Chen, G., Chen, W., Tapponnier, P., and Zhang, B., 2007, Millennial recurrence of large earthquakes on the Haiyuan fault near Songshan, Gansu Province, China: Bulletin of the Seismological Society of America, v. 97, no. 1B, p. 14–34, https://doi.org/10.1785/0120050118.

Liu-Zeng, J., Chen, T., Zhang, P.Z., Zhang, H.P., Zheng, W.J., Ren, Z.K., Liang, S.M., Shen, C.S., and Gan, W.J., 2013, Illuminating the active Haiyuan fault, China, by airborne light detection and ranging: Chinese Science Bulletin, v. 58, p. 41–45 [in Chinese], https://doi.org/10.1360/972012-1526.

Liu-Zeng, J., Shao, Y., Klinger, Y., Xie, K., Yuan, D., and Lei, Z., 2015, Variability in magnitude of paleoearthquakes revealed by trenching and historical records, along the Haiyuan fault, China: Journal of Geophysical Research–Solid Earth, v. 120, no. 12, p. 8304–8333, https://doi.org/10.1002/2015JB012163.

Lu, Y.C., Wang, X.L., and Wintle, A.G., 2007, A new OSL chronology for dust accumulation in the last 130,000 yr for the Chinese Loess Plateau: Quaternary Research, v. 67, no. 1, p. 152–160, https://doi.org/10.1016/j.yqres.2006.08.003.

Mason, D.P., Little, T.A., and Van Dissen, R.J., 2006, Rates of active faulting during late Quaternary fluvial terrace formation at Saxton River, Awatere fault, New Zealand: Geological Society of America Bulletin, v. 118, no. 11–12, p. 1431–1446, https://doi.org/10.1130/B25961.1.

Matrau, R., Klinger, Y., Van der Woerd, J., Liu-Zeng, J., Li, Z., Xu, X., and Zheng, R., 2019, Late Pleistocene–Holocene slip rate along the Hasi Shan restraining bend of the Haiyuan fault: Implication for faulting dynamics of a complex fault system: Tectonics, v. 38, p. 4127–4154, https://doi.org/10.1029/2019TC005488.

McGill, S.F., Owen, L.A., Weldon, R.J., and Kendrick, K.J., 2013, Latest Pleistocene and Holocene slip rate for the San Bernardino strand of the San Andreas fault, Plunge Creek, Southern California: Implications for strain partitioning within the southern San Andreas fault system for the last~35 k.y.: Geological Society of America Bulletin, v. 125, no. 1–2, p. 48–72, https://doi.org/10.1130/B30647.1.

Meade, B.J., Klinger, Y., and Hetland, E.A., 2013, Inference of multiple earthquake-cycle relaxation timescales from irregular geodetic sampling of interseismic deformation: Bulletin of the Seismological Society of America, v. 103, no. 5, p. 2824–2835, https://doi.org/10.1785/0120130006.

Mériaux, A.S., Ryerson, F.J., Tapponnier, P., Van der Woerd, J., Finkel, R.C., Xu, X., Xu, Z., and Caffee, M.W., 2004, Rapid slip along the central Altyn Tagh fault: Morphochronologic evidence from Cherchen He and Sulamu Tagh: Journal of Geophysical Research, v. 109, B06401, https://doi.org/10.1029/2003JB002558.

Mériaux, A.S., Tapponnier, P., Ryerson, F.J., Xu, X.W., King, G., Van der Woerd, J., Finkel, R.C., Li, H.B., Caffee, M.W., Xu, Z.Q., and Chen, W.B., 2005, The Aksay section of the northern Altyn Tagh fault: Tectonic geomorphology, landscape evolution, and Holocene slip rate: Journal of Geophysical Research–Solid Earth, v. 110, no. B4, B04404, https://doi.org/10.1029/2004JB003210.

Mériaux, A.S., Van Der Woerd, J., Tapponnier, P., Ryerson, F.J., Finkel, R.C., Lasserre, C., and Xu, X., 2012, The Pingding segment of the Altyn Tagh fault (91°E): Holocene slip-rate determination from cosmogenic radionuclide dating of offset fluvial terraces: Journal of Geophysical Research–Solid Earth, v. 117, no. B9, B09406, https://doi.org/10.1029/2012JB009289.

Meyer, B., Tapponnier, P., Gaudemer, Y., Peltzer, G., Guo, S., and Chen, Z., 1996, Rate of left-lateral movement along the easternmost segment of the Altyn Tagh fault, east of 96°E (China): Geophysical Journal International, v. 124, p. 29–44, https://doi.org/10.1111/j.1365-246X.1996.tb06350.x.

Meyer, B., Tapponnier, P., Bourjot, L., Metivier, F., Gaudemer, Y., Peltzer, G., Shunmin, G., and Zhitai, C., 1998, Crustal thickening in Gansu-Qinghai, lithospheric mantle subduction, and oblique, strike-slip controlled growth of the Tibet Plateau: Geophysical Journal International, v. 135, no. 1, p. 1–47, https://doi.org/10.1046/j.1365-246X.1998.00567.x.

Middleton, T.A., Walker, R.T., Parsons, B., Lei, Q., Zhou, Y., and Ren, Z., 2016, A major, intraplate, normal-faulting earthquake: The 1739 Yinchuan event in northern China: Journal of Geophysical Research–Solid Earth, v. 121, no. 1, p. 293–320, https://doi.org/10.1002/2015JB012355.

Min, W., Zhang, P., Deng, Q., and Mao, F., 2001, Detailed study of Holocene paleoearthquakes of the Haiyuan active fault: Geological Review (Dizhi Lunping), v. 47, no. 1, p. 75–81.

Oskin, M.E., Le, K., and Strane, M.D., 2007, Quantifying fault-zone activity in arid environments with high-resolution topography: Geophysical Research Letters, v. 34, no. L23, L23S05, https://doi.org/10.1029/2007GL031295.

Oskin, M.E., Arrowsmith, J.R., Corona, A.H., Elliott, A.J., Fletcher, J.M., Fielding, E.J., Gold, P.O., Garcia, J.J.G., Hudnut, K.W., Liu-Zeng, J., and Teran, O.J., 2012, Near-field deformation from the El Mayor–Cucapah earthquake revealed by differential LiDAR: Science, v. 335, no. 6069, p. 702–705, https://doi.org/10.1126/science.1213778.

Ou, Q., Kulikova, G., Yu, J., Elliott, A., Parsons, B., and Walker, R., 2020, Magnitude of the 1920 Haiyuan earthquake reestimated using seismological and geomorphological methods. Journal of Geophysical Research–Solid Earth, v. 125, e2019JB019244, https://doi.org/10.1029/2019JB019244.

Owen, L.A., Spencer, J.Q., Ma, H., Barnard, P.L., Derbyshire, E., Finkel, R.C., Caffee, M.W., and Zeng, Y.N., 2003, Timing of late Quaternary glaciation along the southwestern slopes of the Qilian Shan: Boreas, v. 32, p. 281–291, https://doi.org/10.1080/03009480310001632.

Owen, L.A., Frankel, K.L., Knott, J.R., Reynhout, S., Finkel, R.C., Dolan, J.F., and Lee, J., 2011, Beryllium-10 terrestrial cosmogenic nuclide surface exposure dating of Quaternary landforms in Death Valley: Geomorphology, v. 125, no. 4, p. 541–557, https://doi.org/10.1016/j.geomorph.2010.10.024.

Papanikolaou, I.D., Roberts, G.P., and Michetti, A.M., 2005, Fault scarps and deformation rates in Lazio-Abruzzo, central Italy: Comparison between geological fault slip-rate and GPS data: Tectonophysics, v. 408, no. 1–4, p. 147–176, https://doi.org/10.1016/j.tecto.2005.05.043.

Peltzer, G., Tapponnier, P., Gaudemer, Y., Meyer, B., Guo, S., Yin, K., Chen, Z., and Dai, H., 1988, Offsets of late Quaternary morphology, rate of slip, and recurrence of large earthquakes on the Chang Ma fault (Gansu, China): Journal of Geophysical Research–Solid Earth, v. 93, no. B7, p. 7793–7812, https://doi.org/10.1029/JB093iB07p07793.

Peltzer, G., Tapponnier, P., and Armijo, R., 1989, Magnitude of late Quaternary left-lateral displacements along the north edge of Tibet: Science, v. 246, no. 4935, p. 1285–1289, https://doi.org/10.1126/science.246.4935.1285.

Peltzer, G., Brown, N.D., Mériaux, A.S.B., Van der Woerd, J., Rhodes, E.J., Finkel, R.C., Ryerson, F.J., and Hollingsworth, J., 2020, Stable rate of slip along the Karakax section of the Altyn Tagh fault from observation of inter-glacial and post-glacial offset morphology and surface dating: Journal of Geophysical Research–Solid Earth, v. 125, no. 5, p. e2019JB018893, https://doi.org/10.1029/2019JB018893.

Perrineau, A., Van Der Woerd, J., Gaudemer, Y., Liu-Zeng, J., Pik, R., Tapponnier, P., Thuizat, R., and Rongzhang, Z., 2011, Incision rate of the Yellow River in northeastern Tibet constrained by ^{10}Be and ^{26}Al cosmogenic isotope dating of fluvial terraces: Implications for catchment evolution and plateau building, *in* Gloaguen, R., and Ratschbacher, L., eds., Growth and Collapse of the Tibetan Plateau: Geological Society [London] Special Publication 353, p. 189–219, https://doi.org/10.1144/SP353.10.

Prush, V., and Oskin, M., 2020, A mechanistic erosion model for cosmogenic inheritance in single-clast exposure ages: Earth and Planetary Science Letters, v. 535, 116066, https://doi.org/10.1016/j.epsl.2020.116066.

Putkonen, J., and Swanson, T., 2003, Accuracy of cosmogenic ages for moraines: Quaternary Research, v. 59, no. 2, p. 255–261, https://doi.org/10.1016/S0033-5894(03)00006-1.

Ran, Y., Duan, R., and Deng, Q., 1997, 3-D trench excavation and paleoseismology at Gaowanzi of the Haiyuan fault: Earthquake Geology, v. 19, no. 2, p. 97–107 [in Chinese with English abstract].

Reitman, N.G., Mueller, K.J., Tucker, G.E., Gold, R.D., Briggs, R.W., and Barnhart, K.R., 2019, Offset channels may not accurately record strike-slip fault displacement: Evidence from landscape evolution models: Journal of Geophysical Research–Solid Earth, v. 124, no. 12, p. 13427–13451, https://doi.org/10.1029/2019JB018596.

Ren, Z., Zhang, Z., Chen, T., Yan, S., Yin, J., Zhang, P., Zheng, W., Zhang, H., and Li, C., 2016, Clustering of offsets on the Haiyuan fault and their relationship to paleoearthquakes: Geological Society of America Bulletin, v. 128, no. 1–2, p. 3–18, https://doi.org/10.1130/B31155.1.

Ritz, J.-F., Vassallo, R., Braucher, R., Brown, E.T., Carretier, S., and Bourlès, D.L., 2006, Using in situ–produced ^{10}Be to quantify active tectonics in the Gurvan Bogd mountain range (Gobi-Altay, Mongolia), *in* Alonso-Zarza, A.M., and Tanner, L.H., eds., In Situ–Produced Cosmogenic Nuclides and Quantification of Geological Processes: Geological Society of America Special Paper 415, p. 87–110, https://doi.org/10.1130/2006.2415(06).

Rizza, M., Ritz, J.F., Braucher, R., Vassallo, R., Prentice, C., Mahan, S., McGill, S., Chauvet, A., Marco, S., Todbileg, M., Demberel, S., and Bourles, D., 2011, Slip rate and slip magnitudes of past earthquakes along the Bogd left-lateral strike-slip fault (Mongolia): Geophysical Journal International, v. 186, no. 3, p. 897–927, https://doi.org/10.1111/j.1365-246X.2011.05075.x.

Rodgers, D.W., and Little, T.A., 2006, World's largest coseismic strike-slip offset: The 1855 rupture of the Wairarapa fault, New Zealand, and implications for displacement/length scaling of continental earthquakes: Journal of Geophysical Research–Solid Earth, v. 111, no. B12, B12408, https://doi.org/10.1029/2005JB004065.

Ryerson, F.J., Tapponnier, P., Finkel, R.C., Meriaux, A., Van der Woerd, J., Lasserre, C., Chevalier, M., Xu, X.W., Li, H.B., and King, G.C., 2006, Applications of morphochronology to the active tectonics of Tibet, *in* Alonso-Zarza, A.M., and Tanner, L.H., eds., In Situ–Produced Cosmogenic Nuclides and Quantification of Geological Processes: Geological Society of America Special Paper 415, p. 61–86, https://doi.org/10.1130/2006.2415(05).

Sieh, K.E., 1981, A review of geological evidence for recurrence times of large earthquakes, *in* Simpson, D.W., and Richards, P.G., eds., Earthquake Prediction: An International Review: American Geophysical Union Maurice Ewing Volume 4, p. 181–207, https://doi.org/10.1029/ME004p0181.

Sieh, K.E., and Jahns, R.H., 1984, Holocene activity of the San Andreas fault at Wallace Creek, California: Geological Society of America Bulletin, v. 95, no. 8, p. 883–896, https://doi.org/10.1130/0016-7606(1984)95<883:HAOTSA>2.0.CO;2.

Stewart, N., Gaudemer, Y., Manighetti, I., Serreau, L., Vincendeau, A., Dominguez, S., Mattéo, L., and Malavieille, J., 2018, "3D_Fault_Offsets": A Matlab code to automatically measure lateral and vertical fault offsets in topographic data: Application to San Andreas, Owens Valley, and Hope faults: Journal of Geophysical Research–Solid Earth, v. 123, p. 815–835, https://doi.org/10.1002/2017JB014863.

Stokes, S., Hetzel, R., Bailey, R.M., and Mingxin, T., 2003, Combined IRSL-OSL single aliquot regeneration (SAR) equivalent dose (De) estimates from source proximal Chinese loess: Quaternary Science Reviews, v. 22, no. 10, p. 975–983, https://doi.org/10.1016/S0277-3791(03)00044-1.

Stone, J.O., 2000, Air pressure and cosmogenic isotope production: Journal of Geophysical Research, v. 105, p. 23753–23759, https://doi.org/10.1029/2000JB900181.

Stuiver, M., and Reimer, P.J., 1993, Extended ^{14}C database and revised CALIB 3.0 ^{14}C age calibration program: Radiocarbon, v. 35, no. 1, p. 215–230, https://doi.org/10.1017/S0033822200013904.

Tapponnier, P., and Molnar, P., 1977, Active faulting and tectonics in China: Journal of Geophysical Research, v. 82, no. 20, p. 2905–2930, https://doi.org/10.1029/JB082i020p02905.

Tapponnier, P., Meyer, B., Avouac, J.P., Peltzer, G., Gaudemer, Y., Shunmin, G., Hongfa, X., Kelun, Y., Zhitai, C., Shuahua, C., and Huagang, D., 1990, Active thrusting and folding in the Qilian Shan, and decoupling between upper crust and mantle in northeastern Tibet: Earth and Planetary Science Letters, v. 97, no. 3–4, p. 382–403, https://doi.org/10.1016/0012-821X(90)90053-Z.

Tapponnier, P., Zhiqin, X., Roger, F., Meyer, B., Arnaud, N., Wittlinger, G., and Jingsui, Y., 2001a, Oblique stepwise rise and growth of the Tibet Plateau: Science, v. 294, no. 5547, p. 1671–1677, https://doi.org/10.1126/science.105978.

Tapponnier, P., Ryerson, F.J., Van Der Woerd, J., Mériaux, A.S., and Lasserre, C., 2001b, Long-term slip rates and characteristic slip: Keys to active fault behaviour and earthquake hazard: Comptes Rendus de l'Académie des Sciences, ser. IIA, Earth and Planetary Science, v. 333, no. 9, p. 483–494, https://doi.org/10.1016/S1251-8050(01)01668-8.

Thackray, G.D., Rodgers, D.W., and Streutker, D., 2013, Holocene scarp on the Sawtooth fault, central Idaho, USA, documented through LiDAR topographic analysis: Geology, v. 41, no. 6, p. 639–642, https://doi.org/10.1130/G34095.1.

Tocheport, A., Rivera, L., and Van der Woerd, J., 2006, A study of the 14 November 2001 Kokoxili earthquake: History and geometry of the rupture from teleseismic data and field observations: Bulletin of the Seismological Society of America, v. 96, no. 5, p. 1729–1741, https://doi.org/10.1785/0120050200.

Tong, X., Smith-Konter, B., and Sandwell, D.T., 2014, Is there a discrepancy between geological and geodetic slip rates along the San Andreas fault system?: Journal of Geophysical Research–Solid Earth, v. 119, no. 3, p. 2518–2538, https://doi.org/10.1002/2013JB010765.

Van der Woerd, J., Ryerson, F.J., Tapponnier, P., Gaudemer, Y., Finkel, R., Mériaux, A.S., Caffee, M., Zhao, G., and He, Q., 1998, Holocene left-slip rate determined by cosmogenic surface dating on the Xidatan section of the Kunlun fault (Qinghai, China): Geology, v. 26, p. 695–698, https://doi.org/10.1130/0091-7613(1998)026<0695:HLSRDB>2.3.CO;2.

Van der Woerd, J., Ryerson, F.J., Tapponnier, P., Meriaux, A.S., Gaudemer, Y., Meyer, B., Finkel, R.C., Caffee, M.W., Guoguang, Z., and Zhiqin, X., 2000, Uniform slip-rate along the Kunlun fault: Implications for seismic behaviour and large-scale tectonics: Geophysical Research Letters, v. 27, no. 16, p. 2353–2356, https://doi.org/10.1029/1999GL011292.

Van der Woerd, J., Tapponnier, P.J., Ryerson, F., Meriaux, A.S., Meyer, B., Gaudemer, Y., Finkel, R.C., Caffee, M.W., Guoguan, Z., and Zhiqin, X., 2002, Uniform postglacial slip-rate along the central 600 km of the Kunlun fault (Tibet), from ^{26}Al, ^{10}Be, and ^{14}C dating of riser offsets, and climatic origin of the regional morphology: Geophysical Journal International, v. 148, no. 3, p. 356–388, https://doi.org/10.1046/j.1365-246x.2002.01556.x.

Van der Woerd, J., Klinger, Y., Sieh, K., Tapponnier, P., Ryerson, F.J., and Mériaux, A.-S., 2006, Long-term slip rate of the southern San Andreas fault from ^{10}Be-^{26}Al surface exposure dating of an offset alluvial fan: Journal of Geophysical Research, v. 111, B04407, https://doi.org/10.1029/2004JB003559.

Wang, X., Vandenberghe, D., Yi, S., Vandenberghe, J., Lu, H., Van Balen, R., and Van den Haute, P., 2013, Late Quaternary paleoclimatic and geomorphological evolution at the interface between the Menyuan Basin and the Qilian Mountains, northeastern Tibetan Plateau: Quaternary Research, v. 80, no. 3, p. 534–544, https://doi.org/10.1016/j.yqres.2013.08.004.

Weldon, R., 1986, The Late Cenozoic Geology of Cajon Pass: Implications for Tectonics and Sedimentation along the San Andreas Fault [Ph. D. thesis]: Pasadena, California, California Institute of Technology, 400 p.

Weldon, R., and Sieh, K.E., 1985, Holocene rate of slip and tentative recurrence interval for large earthquakes on the San Andreas fault, Cajon Pass, Southern California: Geological Society of America Bulletin, v. 96, p. 793–812, https://doi.org/10.1130/0016-7606(1985)96<793:HROSAT>2.0.CO;2.

Weldon, R., Scharer, K., Fumal, T., and Biasi, G., 2004, Wrightwood and the earthquake cycle: What a long recurrence record tells us about how faults work: GSA Today, v. 14, no. 9, p. 4–10, https://doi.org/10.1130/1052-5173(2004)014<4:WATECW>2.0.CO;2.

Wells, D., and Coppersmith, K., 1994, New empirical relationships among magnitude, rupture length, rupture width, rupture area, and surface displacement: Bulletin of the Seismological Society of America, v. 84, no. 4, p. 974–1002.

Wesnousky, S.G., 2006, Predicting the endpoints of earthquake ruptures: Nature, v. 444, no. 7117, p. 358–360, https://doi.org/10.1038/nature05275.

Wu, G.J., Pan, B.T., Guan, Q.Y., Wang, J.M., and Zhao, Z.J., 1998, Climatic changes in the north piedmont of eastern Qilian mountains since 10 ka B.P.: Journal of Desert Research, v. 18, no. 3, p. 1993–200 [in Chinese with English abstract].

Xiang, H.F., Guo, S.M., Zhang, B.L., Zhang, W.X., Yasutaka, I., and He, H.L., 1998, Active features of the eastern Liupanshan piedmont reverse fault zone since late: Seismology and Geology (Dizhen Dizhi), v. 20, no. 4, p. 321–327 Quaternary [in Chinese].

Xu, X., Yu, G., Ma, W., Klinger, Y., and Tapponnier, P., 2008, Rupture behavior and deformation localization of the Kunlunshan earthquake (Mw 7.8) and their tectonic implications: Science in China, ser. D, Earth Sciences, v. 51, no. 10, p. 1361–1374, https://doi.org/10.1007/s11430-008-0099-z.

Yao, W.Q., Liu-Zeng, J., Oskin, M.E., Wang, W., Li, Z.F., Prush, V., Zhang, J.Y., Tang, M.Y., Shao, Y.X., Yuan, Z.D., Han, L.F., and Klinger, Y., 2019, Re-evaluation of the late Pleistocene slip rate of the Haiyuan fault near Songshan, Gansu Province, China: Journal of Geophysical Research–Solid Earth, v. 124, no. 5, p. 5217–5240, https://doi.org/10.1029/2018JB016907.

Yıkılmaz, M.B., Turcotte, D.L., Heien, E.M., Kellogg, L.H., and Rundle, J.B., 2015, Critical jump distance for propagating earthquake ruptures across step-overs: Pure and Applied Geophysics, v. 172, no. 8, p. 2195–2201, https://doi.org/10.1007/s00024-014-0786-y.

Yuan, D.Y., Liu, B.C., Lv, T.Y., He, W.G., and Liu, X.F., 1997, Palaeoearthquake features along the eastern segment of north Qilianshan active fault zone: South China Journal of Seismology, v. 17, no. 2, p. 24–31 [in Chinese].

Yuan, D.Y., Liu, B.C., Lv, T.Y., He, W.G., Liu, X.F., and Gan, W.J., 1998, Study on the sectionation of the eastern section of north Qilianshan active fault zone: Northwestern Seismological Journal, v. 20, no. 4, p. 27–34 [in Chinese].

Zechar, J.D., and Frankel, K.L., 2009, Incorporating and reporting uncertainties in fault slip rates: Journal of Geophysical Research, v. 114, B12407, https://doi.org/10.1029/2009JB006325.

Zhang, J., Nottebaum, V., Tsukamoto, S., Lehmkuhl, F., and Frechen, M., 2015, Late Pleistocene and Holocene loess sedimentation in central and western Qilian Shan (China) revealed by OSL dating: Quaternary International, v. 372, p. 120–129, https://doi.org/10.1016/j.quaint.2014.12.054.

Zhang, P., Molnar, P., Burchfiel, B.C., Royden, L., Wang, Y., Deng, Q., Song, F., Zhang, W., and Jiao, D., 1988a, Bounds on the Holocene slip rate along the Haiyuan fault, north-central China: Quaternary Research, v. 30, p. 151–164, https://doi.org/10.1016/0033-5894(88)90020-8.

Zhang, P., Molnar, P., Weigi, Z., Qidong, D., Yipeng, W., Burchfiel, B.C., Fangmin, S., Royden, L., and Decheng, J., 1988b, Bounds on the average recurrence interval of major earthquakes along the Haiyuan fault in north-central China: Seismological Research Letters, v. 59, no. 3, p. 81–89, https://doi.org/10.1785/gssrl.59.3.81.

Zhang, P., Min, W., Deng, Q., and Mao, F., 2003, Paleoearthquake rupture behavior and recurrence of great earthquakes along the Haiyuan fault, northwestern China: Science China, ser. D, v. 46, p. 705–713.

Zhang, P.Z., Molnar, P., and Xu, X., 2007, Late Quaternary and present-day rates of slip along the Altyn Tagh fault, northern margin of the Tibetan Plateau: Tectonics, v. 26, TC5010, https://doi.org/10.1029/2006TC002014.

Zheng, D.W., Zhang, P.Z., Wan, J.L., Yuan, D.Y., Li, C.Y., Yin, G.M., Zhang, G.L., Wang, Z.C., Min, M., and Chen, J., 2006, Rapid exhumation at ca. 8 Ma on the Liupan Shan thrust fault from apatite fission-track thermochronology: Implications for growth of the northeastern Tibetan Plateau margin: Earth and Planetary Science Letters, v. 248, no. 1–2, p. 198–208, https://doi.org/10.1016/j.epsl.2006.05.023.

Zheng, W.J., Zhang, P.Z., He, W.G., Yuan, D.Y., Shao, Y.X., Zheng, D.W., Ge, W.P., and Min, W., 2013, Transformation of displacement between strike-slip and crustal shortening in the northern margin of the Tibetan Plateau: Evidence from decadal GPS measurements and late Quaternary slip rates on faults: Tectonophysics, v. 584, p. 267–280, https://doi.org/10.1016/j.tecto.2012.01.006.

Zielke, O., Arrowsmith, J.R., Grant-Ludwig, L.B., and Akciz, S.O., 2010, Slip in the 1857 and earlier large earthquakes along the Carrizo section, San Andreas fault: Science, v. 327, p. 1119–1122, https://doi.org/10.1126/science.1182781.

Zielke, O., Arrowsmith, J.R., Grant-Ludwig, L.B., and Akciz, S.O., 2012, High resolution topography-derived offset along the 1857 Fort Tejon earthquake rupture trace, San Andreas fault: Bulletin of the Seismological Society of America, v. 102, no. 3, p. 1135–1154, https://doi.org/10.1785/0120110230.

Zielke, O., Klinger, Y., and Arrowsmith, J.R., 2015, Fault slip and earthquake recurrence along strike-slip faults—Contributions of high-resolution geomorphic data: Tectonophysics, v. 638, p. 43–62, https://doi.org/10.1016/j.tecto.2014.11.004.

Zinke, R., Dolan, J.F., Van Dissen, R., Grenader, J.R., Rhodes, E.J., McGuire, C.P., Langridge, R.M., Nicol, A., and Hatem, A.E., 2015, Evolution and progressive geomorphic manifestation of surface faulting: A comparison of the Wairau and Awatere faults: South Island, New Zealand: Geology, v. 43, no. 11, p. 1019–1022, https://doi.org/10.1130/G37065.1.

Zinke, R., Dolan, J.F., Rhodes, E.J., Van Dissen, R., and McGuire, C.P., 2017, Highly variable latest Pleistocene–Holocene incremental slip rates on the Awatere fault at Saxton River, South Island, New Zealand, revealed by LiDAR mapping and luminescence dating: Geophysical Research Letters, v. 44, p. 11301–11310, https://doi.org/10.1002/2017GL075048.

Science Editor: Rob Strachan
Associate Editor: Bernhard Grasemann

Manuscript Received 3 December 2019
Revised Manuscript Received 16 August 2020
Manuscript Accepted 5 September 2020

Printed in the USA